A polycrystalline damage model applied to an anisotropic aluminum alloy 2198 under non-proportional load path changes

Xiang Kong, Thilo F. Morgeneyer, Djamel Missoum-Benziane, Gilles Rousselier

A polycrystalline damage model applied to an anisotropic aluminum alloy 2198 under non-proportional load path changes

Xiang Kong[a], Thilo F. Morgeneyer[a], Djamel Missoum-Benziane[a], Gilles Rousselier[a,*]

[a] *Mines Paris, PSL University, Centre des Matériaux, CNRS UMR 7633, Evry, France*

Abstract

A ductile damage model, which fully couples classical void growth at high stress triaxiality and Coulomb ductile model at the slip system scale at low stress triaxiality, was applied for the sheet specimens in an anisotropic aluminum alloy under non-proportional load path changes. The Coulomb model combines the resolved normal and shear stresses for each slip plane and directions. A Reduced Texture Methodology (RTM) was used to provide computational efficiency and this approach involved a significant reduction in the number of representative crystallographic orientations. The 12-grain model using 12 crystallographic orientations was validated for non-proportional load path change experiments. The model was calibrated in plasticity using single element calculations under proportional tension, shear and non-proportional 'shear to tension' (ST) loadings. Next, the damage parameters were calibrated against the proportional loading shear and tension experimental results using 3D mesh full-size calculations. The calibrated model successfully predicted non-proportional failure. Locally, the damage indicator maxima coincided with the damage location where the damage features were observed via experimental 3D imaging (computed tomography).

Keywords: `Ductile damage, Non-proportional load, Polycrystalline model, Aluminum alloy, Computed tomography`

1. Introduction

Ductile fracture of metals is known for its mechanism of void nucleation-growth-coalescence driven by high stress triaxiality [Pineau et al., 2016]. Recently, more researches have focused on another mechanism especially at low stress triaxiality or shear dominated loading conditions. Many ex-

*Corresponding author
Email address: `gilles.rousselier@minesparis.psl.eu` (Gilles Rousselier)

perimental works [Bao and Wierzbicki, 2004, Barsoum and Faleskog, 2007, Dunand and Mohr, 2011, Papasidero et al., 2014, 2015, Roth and Mohr, 2016, Gross and Ravi-Chandar, 2016, Kong et al., 2023a, Tancogne-Dejean et al., 2021, Brünig et al., 2021, Buljac et al., 2023] have been performed to investigate the ductile failure under proportional and/or non-proportional shear-dominated loading paths. In the absence of high stress triaxiality, void growth is limited with no obvious increase for the main damage indicator, void volume fraction, during intense shearing. Lode parameters, as the third invariant of the stress tensor, have been developed and considered as a suitable additional variable to identify the mechanical state [Bai and Wierzbicki, 2008, Morin et al., 2017, Lou et al., 2020]. Experimentally, shear damage features have been observed in laboratory macro specimens via 2D *in situ* SEM [Li et al., 2011, Khan and Liu, 2012a, Achouri et al., 2013, Papasidero et al., 2014, Gross and Ravi-Chandar, 2016] and 3D X-ray synchrotron imaging [Morgeneyer et al., 2014, Roth et al., 2018, Tancogne-Dejean et al., 2021, Kong et al., 2022, 2023b, Buljac et al., 2023]. Voids that nucleated on particles, including intermetallic particle debris and matrix particle debonding, are commonly seen to rotate and flatten till coalescence in ductile metals (e.g., aluminum alloys and steels). Despite the difficulties in terms of the observation and measurement of the secondary voids due to their small dimension, it has been shown that these small voids can lead to changes in void volume fraction [Brünig et al., 2014, Roth et al., 2018, Tancogne-Dejean et al., 2021]. Another feature of grain-related flat cracks (transgranular and intergranular) without attaching particles is particularly found in an Al-Cu-Li alloy 2198, which turns out to be detrimental in tension [Chen, 2011, Morgeneyer et al., 2014, Rousselier et al., 2017] and shear loadings [Kong et al., 2022, 2023b, Buljac et al., 2023]. The crack is supposed to propagate in the best orientated slip system of each grain [Chen, 2011]. Furthermore, the damage mechanism under non-proportional load path change is even more complicated and the mechanisms cannot clearly be established by observing fracture surfaces [Papasidero et al., 2015, Brünig et al., 2021, Kong et al., 2023a]. The stress state plays an important role in ductile fracture and has been accounted for in the investigations over the last decade [Stoughton and Yoon, 2011, Khan and Liu, 2012a, Brünig et al., 2014, Li et al., 2017, Lou and Yoon, 2018, Lou et al., 2020] as well as anisotropic effects, strain rate and temperature [Khan and Baig, 2011, Khan and Liu, 2012b, 2016, Lou and Yoon, 2018, Pandya et al., 2020, Park et al., 2020, Yang et al., 2022].

The classical Gurson [1977] model is not suitable for predicting shear failure under zero mean stress where the loss of load carrying capacity is associated with void growth and softening, and

thus absent under zero stress triaxiality. The Gurson model was extensively modified so that it accommodates failure under intense void shearing by letting the additional damage parameter increase [Nahshon and Hutchinson, 2008] or depending on the third stress invariant [Xue, 2008, Xue and Wierzbicki, 2008] at zero stress triaxiality. The void shearing phenomenon was not observed in the present aluminum alloy with negligible initial-porosity [Chen, 2011, Kong et al., 2022]. Simulations using a micromechanical unit cell with pre-existing cylindrical void have been performed to study shear ductile failure [Tvergaard, 2008, 2009, Nielsen and Tvergaard, 2011, Nielsen et al., 2012], and they found the void closure leading to micro-cracks that rotate in the shear field, instead of void growth to coalescence. Nielsen and Tvergaard [2011] analyzed the shear failure mechanism of primary voids and studied the effect of smaller secondary damage that exists with nucleation in the ligaments between large primary voids that coalesce during intense shearing. Nielsen et al. [2012] performed a 3D cell-unit simulation with spherical voids where they found a good agreement between 2D results and 3D predictions when the void volume is kept constant. Tekoglu and Koçhan [2022] explored the anisotropic effect under complex shear loads using unit cell calculations. For unit cells with single void and random spherical voids, a zone of reduced ductility as minimum strain to failure was found under generalized shear loading conditions (i.e., Lode parameter equals 0) [Cadet et al., 2021, 2022]. In these works, although damage evolution is no longer related to void volume fraction, whereas closure of existing void was predicted in unit cell studies during shearing, the numerical model combined the shear softening due to void distortion and inter-void linking at zero stress triaxiality. On the other hand, Madou and Leblond proposed an alternative extension of the Gurson model, modeling void shape variation from spherical to ellipsoidal and void rotation [Madou and Leblond, 2012a,b, 2013, Madou et al., 2013]. A second porosity variable g contributes to the material softening with the usual one f being substituted by $f+g$ in the plastic potential. The second porosity can characterize the detrimental effect of voids during shear in case f is close to zero. Morin et al. [2016] applied this ML model to micromechanical simulations under shear with initial voids of different shape. Morin et al. [2017] applied this model to the so-called *butterfly* macro specimen under shear loading with comparison to experiments in Dunand and Mohr [2011], demonstrating that the complex model can be used in finite element calculations. A recent work also applied the micromechanical ML model to simulate forming failure under shear loading, where the model accounting for void shape effects is able to reproduce the shear failure [Tajdary et al., 2022].

Aiming to represent an anisotropic plastic behavior, the yield function proposed by Bron and Besson [2004], an extension of the functions given in [Karafillis and Boyce, 1993, Barlat et al., 1991], satisfactorily described yield anisotropy and Lankford coefficient simultaneously in all orientations. The macroscopic plasticity model has been applied to macro specimens at large strain under complex non-proportional load path changes [Kong et al., 2023a]. However, it is difficult with macro-plasticity to model the plastic anisotropy that depends on grain orientations at the microscale (texture), the non-proportional loadings related to cross-hardening between slip systems and other micromechanisms, and the various damage mechanisms that all originate at the microscale. For the target material AA2198-T8R with negligible initial porosity, since the classic particle-related void damage growth is missing under shear and the transgranular crack is supposed to propagate in the best orientated slip system [Chen, 2011, Kong et al., 2022], shear fracture can occur by shear localization at the grain level, and then propagates in the aggregate. A large amount of plastic strain is necessary prior to shear localization and fracture. Two distinct slip rates for each slip systems are considered: the usual slip rate and an additional "damage" slip rate activated at large strains [Rousselier and Luo, 2014] in order to model the phenomenon. Cailletaud [1987, 1992] used the *physics related* hardening variables from the microscale (e.g., local slip rate) to represent a complex macroscopic response. A localization process gives the local stress in each grain and the resolved stress on each slip system based on the self-consistent homogenization scheme. Haouala et al. [2018] investigated the effect of grain size on the mechanical response based on computational homogenization of the polycrystal behavior. Crystal plasticity finite element method (CPFEM) applied crystal plasticity directly at the Gauss point scale of polycrystalline aggregates. It has been employed on a periodic unit cell in simulating and assessing grain interactions [Gérard et al., 2009, Roters et al., 2010, Kanjarla et al., 2010]. Frodal et al. [2021] applied CPFEM to different micro tensile specimens. However, this method requires a very large computation time, where 300-800 hours with 24 cores are needed even with a simple damage model $\sigma_{eff}=\sigma/(1\text{-}D)$ for micro specimens, not to mention macro samples of complex geometry. Parameter calibration requires tens or hundreds of finite element simulations and computational cost reduction is imperative.

Polycrystalline plasticity is less *physical* than CPFEM, but computation time can be remarkably reduced. The Reduced Texture Methodology (RTM), which limits the number of representative crystallographic orientations, is used to provide computation efficiency for numerical applications [Rousselier and Leclercq, 2006, Rousselier et al., 2009, 2010, 2012]. The Rousselier porous plasticity

model can be embedded into the polycrystalline framework [Méric et al., 1991, Cailletaud, 1987, 1992] with plasticity and damage models at the slip system scale, for instance, the Coulomb ductile fracture model [Rousselier and Luo, 2014] (applied to *butterfly* specimen) as well as the nucleation and growth models of very small voids as second population at the slip band scale [Rousselier, 2021] (applied to *Kahn* specimen). 8 to 15 representative grain orientations were chosen to dramatically reduce the CPU time. Texture can be accurate if texture parameters are calibrated. Rousselier [2022] added a Lode-dependent second porosity variable g accounting for stress softening under shear-dominated loadings.

The objective of this paper is to calibrate the mechanism-based model under proportional loadings and to predict grain-related damage behavior of an aluminum alloy 2198-T8R under non-proportional load paths. The Coulomb-Rousselier-Luo (CRL) model, which combines Coulomb slips and classic void growth in the framework of RTM-based polycrystalline plasticity, is presented in Section 2. The material, model calibration strategy and plasticity calibration results are given in Section 3. The model application to a laboratory sheet specimen under different non-proportional load path changes is assessed in Section 4 in terms of macroscopic stress-strain curves as well as the local strain and damage fields. The discussion in Section 5 deals with the comparison between experimental damage observation and numerical predictions as well as the effects of predictive different pre-loadings on ductility. Section 6 ends with conclusions and perspectives. Abbreviations used in this paper are summarized in Tab.1.

2. Constitutive modeling

In this work, A, $\vec{A}$, $\underline{A}$, $\underline{\underline{A}}$ denote a scalar, a vector, a second order tensor and a fourth order tensor respectively. Upper-case symbols (e.g. $\underline{\Sigma}$, $\underline{E}^p$uniform) represent mechanical variables at the macroscopic scale while lower-case symbols (e.g. $\underline{\sigma}$, $\underline{\varepsilon}$, $\underline{\beta}$, τ, γ...) are at the microscopic scales. All the equations are written in a material embedded co-rotational frame [Rousselier et al., 2009, 2010, 2012]. In the finite element analysis, a finite strain frame using the rotation tensor is defined in Appendix A.

A self-consistent polycrystalline model [Méric et al., 1991, Cailletaud, 1992] is the backbone of the constitutive model. The physics-based plasticity succeeds in describing the plastic anisotropy and yield surface distortion, which enables to predict complex behaviors in complex load paths.

Abbreviation	Definition
AA	Aluminum alloy
BB model	Bron-Besson model [Bron and Besson, 2004]
CI	Crack initiation
CPFEM	Crystal plasticity finite element method
CRL model	Coulomb-Rousselier-Luo model [Rousselier and Luo, 2014]
DIC	Digital image correlation
FCC	Face centered cubic
ML model	Madou-Leblond model [Madou and Leblond, 2012a,b, 2013]
ROI	Region of interest
RTM	Reduced texture methodology
SE	End of shear pre-load
SO	Shear-only
SEM	Scanning electron microscope
ST	Shear to tension
TE	End of tension pre-load
TO	Tension-only
TS	Tension to shear
PC model	Polycrystalline model

Table 1: List of abbreviations.

2.1. The self-consistent polycrystalline model

In the self-consistent method, each of N *grains* is considered as an inclusion in the homogeneous equivalent material, which represents a set of physical grains with close crystallographic orientations (or phase in the literature). The macroscopic stress $\underline{\Sigma}$ and plastic strain $\underline{E}^p$ are defined as the homogenization of every *grain* g with a volume fraction f_g in all N *grains*:

$$\underline{\Sigma} = \sum_{g=1}^{N} f_g \underline{\sigma}_g \quad \text{with} \quad \sum_{g=1}^{N} f_g = 1 \tag{1}$$

$$\underline{E}^p = \sum_{g=1}^{N} f_g \underline{\varepsilon}_g^p \quad \text{with} \quad \sum_{g=1}^{N} f_g = 1 \tag{2}$$

$$\underline{\varepsilon}_g^e \equiv \underline{E}^e = (\frac{1+\nu}{E}\underline{\underline{1}} - \frac{\nu}{E}\underline{1}\otimes\underline{1}) : \underline{\Sigma} \tag{3}$$

where E, ν stand for Young's modulus and Poisson's ratio in the case of isotropic elasticity.

In order to establish a relation between the homogenized stress at the macroscopic scale $\underline{\Sigma}$ and microscopic stress of each grain $\underline{\sigma}_g$, the scale transition rule (also called 'β rule') is used [Cailletaud, 1987, 1992]. It provides a general method to model the elastic-to-plastic transition of intergranular deformations by introducing an intermediate deviatoric strain tensor $\underline{\beta}_g$:

$$\underline{\sigma}_g = \underline{\Sigma} + C(\underline{B} - \underline{\beta}_g) \quad \text{with} \quad \underline{B} = \sum_{g=1}^{N} f_g \underline{\beta}_g \tag{4}$$

$$\dot{\underline{\beta}}_g = \dot{\underline{\varepsilon}}_g^p - \underline{\underline{D}} : \underline{\beta}_g \|\dot{\underline{\varepsilon}}_g^p\| \quad \text{where} \quad \|\dot{\underline{\varepsilon}}_g^p\| = \sqrt{\frac{2}{3}\dot{\underline{\varepsilon}}_g^p : \dot{\underline{\varepsilon}}_g^p} \tag{5}$$

Here the scalar modulus C is similar to the elastic shear modulus $\mu = E/2(1+\nu)$ according to Kröner theory [Kroner, 1961]. The second invariant $\|\dot{\underline{\varepsilon}}_g^p\|$ represents the von Mises equivalent strain rate for each grain g. Sai et al. [2006] proposed the fourth order tensor $\underline{\underline{D}}$ for anisotropic materials and 10 independent components D_{ij} are needed as explained in Appendix B.

The RTM can make use of any polycrystalline plasticity model with a very small number of crystallographic orientations. *Grain* can be represented with a set of texture parameters including Euler angles (φ_1, Φ, φ_2) and volume fraction $frac$, where its orientation is denoted from the material frame with three successive rotations: rotation φ_1 around the axis 3 of the material reference frame, rotation Φ around the updated axis 1 and rotation φ_2 around the updated axis 3. In this study for orthotropic aluminum sheet, each texture component consists of four symmetric grain orientations as (φ_1, Φ, φ_2), (-φ_1, Φ, -φ_2), (-φ_1, -Φ, -φ_2), (φ_1, -Φ, φ_2).

It has to be remarked that the mean field self-consistent model in the present work does not account for (i) the grain location in the aggregate, (ii) the grain size effect and (iii) the strain and stress gradients within grains (e.g., grain boundary effect is neglected).

2.2. The single crystal plasticity

This subsection presents the constitutive equations at the scale of a single crystal. The single crystal model relates the slip rate $\dot{\gamma}_s = 2\dot{\epsilon}_s$ and the resolved shear stress τ_s of each slip system (s

$= 1$ to M) where the index g for each grain is omitted in the following.

The resolved shear stress τ_s at the given slip system number s is defined:

$$\tau_s = \underline{\sigma}_g : \underline{m}_s \quad \text{with} \quad \underline{m}_s = (\vec{l}_s \otimes \vec{n}_s + \vec{n}_s \otimes \vec{l}_s)/2 \tag{6}$$

where the orientation tensor $\underline{m}_s$ is defined with slip plane normal vector $\vec{n}_s$ and slip direction vector $\vec{l}_s$ in this plane.

For the FCC crystallographic structure in this study, octahedral slip systems $\{111\}\langle\bar{1}10\rangle$ are considered with $M = 12$. A phenomenological Norton-like viscoplastic model is used for the constitutive equations of each slip system:

$$\dot{\gamma}_s = \dot{\nu}_s Sign(\tau_s - X_s) \tag{7}$$

$$\dot{\nu}_s = |\dot{\gamma}_s| = \max[0, (\frac{|\tau_s - X_s| - r_s}{K_s})^{n_s}] \tag{8}$$

$$r_s = r_s(\nu_s, \nu_t), \forall t \neq s \tag{9}$$

For each slip system, an internal variable $r_s = r_s(\nu_s, \nu_t)$ is introduced for isotropic hardening, which depends on the cumulative slip ν_t of the M slip systems. Kinematic hardening part is available but not considered in this study, because experimental data to calibrate the parameters is not available. The viscoplastic flow reaches the rate-independent limit for large n_s and small K_s. For the FCC crystallographic structures, the same viscosity parameters K_s=K_{vp} and n_s=n_{vp} are used for all octahedral slip systems.

The strain can be very large (e.g. greater than 0.6) in shear experiments [Tancogne-Dejean et al., 2021, Kong et al., 2023a, Buljac et al., 2023]. Therefore, the dislocation structures at large strain have to be reorganized and modeled. Luo and Rousselier [2014] proposed a simple method to model the hardening matrix evolution with plastic strain. The isotropic hardening behavior is controlled by three (i=1,2,3) non-linear exponential terms as following:

$$r_s = R + \sum_{i=1}^{3} Q^i \sum_{t=1}^{M} H_{st}^i [1 - \exp(-b^i \nu_t)] \tag{10}$$

where R is the initial critical resolved shear stress. The 12×12 symmetric hardening matrices H_{st}^i only depends on six independent components h_1^i to h_6^i for each hardening term. For brevity, more information about the hardening matrix H_{st}^i is given in Appendix C.

The grain plastic strain rate is:

$$\underline{\dot{\varepsilon}}^p = \sum_{s=1}^{M} \underline{m}_s \dot{\gamma}_s \tag{11}$$

Texture evolution can be modeled with the RTM [Rousselier et al., 2009, 2010]. Although it was not used in this work considering the need for large time-consuming parameter re-calibration, it has been tried for a micro specimen in Appendix D.

2.3. The Coulomb fracture model at the slip system scale

In polycrystalline metals, in the absence of hydrostatic stress for classic particle-related void damage growth under shear loading, grain-related shear flat cracks have been observed [Luo and Rousselier, 2014, Kong, 2022] in the localization zone. Instead of rough dimples in tension-dominated loading, the flat fracture surface of aluminum alloy 2198-T8R under shear is seen in Fig.1.

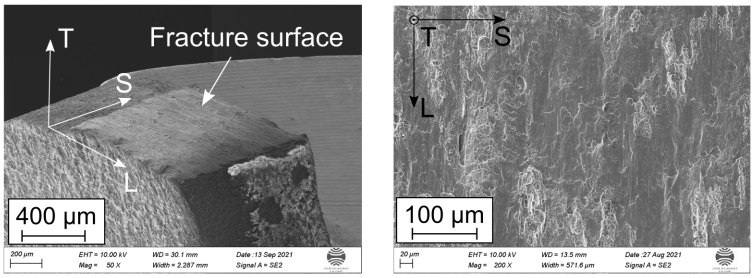

Figure 1: The flat fracture surface of aluminum alloy 2198-T8R under shear loading adapted after Kong et al. [2023a].

In order to model this phenomenon at the slip system scale, the total slip rate, consisting of the classical slip rate $\dot{\gamma}_s$ for strain hardening and an additional Coulomb slip rate $\dot{\gamma}_s^C$ for damage effect activated at large strains, is proposed:

$$\dot{\gamma}_s^{tot} = \dot{\gamma}_s + \dot{\gamma}_s^C \tag{12}$$

At the slip system scale, the only two stress components are resolved shear stress τ_s and normal stress σ_{ns} normal to the slip plane. Both affect the second slip rate activation according to Coulomb criterion with parameters c_0 in Eq.14 and R_0, Q_0 in Eq.15 that defines the strain-softening and the dissipated energy in ductile fracture. r_s^C is a critical value, which decides the Coulomb slip activation.. The viscosity parameters K_0, n_0 are set equal to K_s, n_s in Eq. 8.

$$\dot{\nu}_s^C = \dot{\gamma}_s^C sign(\tau_s) \tag{13}$$

$$\dot{\nu}_s^C = \max[0, (\frac{|\tau_s| + c_0\sigma_{ns} - r_s^C}{K_0})^{n_0}] \tag{14}$$

$$r_s^C = R_0 + Q_0[1 - \exp(-b_0\nu_s^C)] \tag{15}$$

A combined damage variable d is defined to quantify damage extent with maximal Coulomb slip γ_{max}^C and porosity f:

$$d = \sqrt{(\frac{\gamma_{max}^C}{\gamma_u})^2 + (\frac{f}{f_u})^2} \tag{16}$$

where γ_u and f_u are ultimate values set as 3 and 0.25 respectively in this study. In the related finite element computation, the broken criterion is that the Gauss point will be regarded as *broken* state if its d reaches 1. For both damage models, softening is already very large at values much smaller than γ_u and f_u. At d=1, the material has completely lost its load-carrying capacity.

2.4. Classical void damage for particle-related porosity growth

Porous plasticity is coupled with polycrystalline plasticity [Rousselier and Leclercq, 2006, Luo and Rousselier, 2014, Rousselier and Luo, 2014] where Rousselier and Leclercq [2006] proposed an additional *grain* g=0 (G0) with a variable void volume fraction f. The volume fraction of the classical *grains* (g=1 to N) is (1-f)f_g in stead of f_g. Different from Eq.2, once f is added, the homogenized strain rate at the macroscopic scale is written as:

$$\underline{\dot{E}}^p = (1-f)\sum_{g=1}^{N} f_g \underline{\varepsilon}_g^p + f\dot{\varepsilon}_m^p \underline{1} = \underline{\dot{E}}_{dev} + \dot{E}_m^p \underline{1} \tag{17}$$

where the plastic mean strain is $\varepsilon_m^p = trace(\underline{\varepsilon}^p)/3$.

The Gurson model [Gurson, 1977] as well as its extensions: the GTN model [Tvergaard, 1981, Tvergaard and Needleman, 1984] and other derived models [Nahshon and Hutchinson, 2008] are widely used in applications. However, they are not easy to reformulate within the polycrystalline plasticity framework because of their quadratic formulation in the deviatoric stress space. The Rousselier model [Rousselier, 2001, 1987, 1981, Rousselier and Luo, 2014] is selected in this study.

The viscoplastic yield condition for a polycrystalline material is:

$$\frac{\Sigma_{eq}}{1-f} - (\sum_{g=1}^{N} f_g \underline{\sigma}_g)_{eq} + D_1 f \sigma_1 \exp(\frac{\Sigma_m^*}{(1-f)\sigma_1}) = 0 \tag{18}$$

where Σ_{eq} is the von Mises equivalent stress and Σ_m is the mean (or hydrostatic) stress. D_1 and σ_1 are material parameters. In this study, the void growth is assumed to be isotropic.

The void volume fraction rate $\dot{f}$ indicates the sum of a first term due to the mass conservation law and a second term for void nucleation:

$$\dot{f} = 3(1-f)\dot{E}_m^p + A\dot{E}_{eq}^p \tag{19}$$

Morgeneyer et al. [2009] assumed A can be constant between two values of E_{eq}^p and equal to zero otherwise while Chu and Needleman [1980] gave the factor A using a Gaussian function of $\dot{E}_{eq}^p$ with parameters f_N,σ_N and E_N:

$$A = \frac{f_N}{\sigma_N\sqrt{2\pi}} \exp[-(\frac{E_{eq}^p - E_N}{\sigma_N\sqrt{2}})^2] \tag{20}$$

In this present work, the parameters are set D_1=2, σ_1=350 MPa in Eq.18 and f_N=0.0034, σ_N=0.02, E_N=0.10 in Eq.20 as previous work in Rousselier [2021] for the same aluminum alloy. The damage dependence on the third invariant of the stress tensor [Xue and Wierzbicki, 2008] and the additional void rate for shear loadings proposed by [Nahshon and Hutchinson, 2008] are not considered because the shear induced mechanism of void rotation and flattening (leading to void coalescence) was not observed in the present aluminum alloy.

3. Material and plasticity calibration

3.1. Material

The target material in this study is an aluminum-copper-lithium alloy 2198 in its recrystallized state after T851 temper condition. The 2 mm thick rolled sheet is supplied by Constellium. This material has a limited initial porosity (< 0.04 vol%) compared to other aerospace aluminum alloys (AA2139 in Morgeneyer et al. [2009] and AA2024 in Tancogne-Dejean et al. [2021]). The mean volume fraction of intermetallic particles is around 0.34%. The yield strength is 440 MPa and the ultimate tensile strength is 500 MPa. Moderate in-plane plastic anisotropy is found in different loading directions (L: rolling direction, T: transverse direction and D: 45° from the rolling direction around the thickness direction) [Chen, 2011]. However, the Lankford ratios ($L_k \approx 0.5 < 1$), defined as the ratio of the true in-plane strain in width direction ε_w over the strain through the thickness ε_s, exhibit a significant plastic anisotropy.

As presented in Fig.2, the macro and micro specimens were loaded not only in proportional loading but also in non-proportional loading at room temperature. Proportional tests such as (a) uniaxial tension (UT) tests in different loading directions and (b) notched tensile (NT) tests in L and T, were conducted on the 2 mm thick macro specimens. In addition, micro experiments including (d) shear-only (SO) and (e) tension-only (TO) were carried out with the 1 mm thick micro specimens. Non-proportional tests such as 'shear to tension' (ST) and 'tension to shear' (TS) were carried out on the same series cross-shaped specimens in Fig.2 (c). This means that the specimen was under the first loading and then unloaded before turning to the second loading. These experimental data are presented in detail and analyzed in Kong et al. [2023a]. Micro 1mm thick specimens were manufactured from 2 mm thick raw sheet by the means of electrical discharge machining (EDM). The grain shape and size do not change.

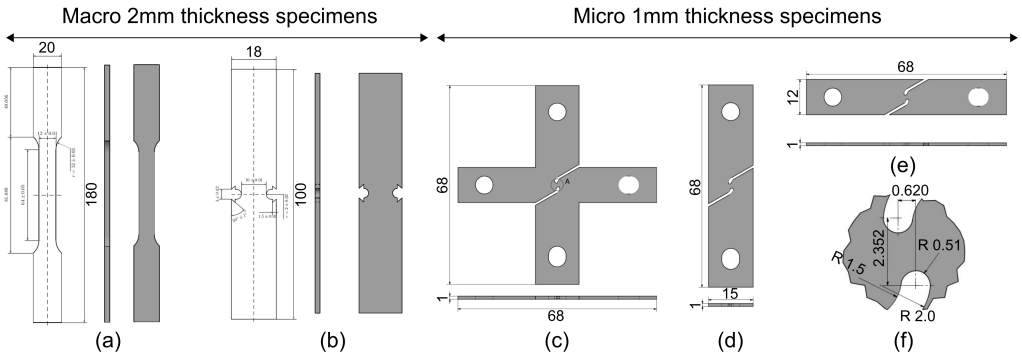

Figure 2: Macro specimen geometries with 2 mm thickness: (a) Uniaxial-tension (UT), (b) Notched-tension (NT2) and micro specimen geometries with $t_0 = 1$ mm thickness: (c) Shear-tension cruciform for non-proportional loadings, (d) Shear-only (SO), (e) Tension-only (TO) samples and (f) the detailed geometry of the region of interest (ROI), where the area of minimum ligament is $S_0 = w_0 t_0$ ($t_0 = 1$ mm and $w_0 = 1.4$ mm for micro specimens in this study) after Kong et al. [2023a].

In order to measure the deformation in the region of interest (ROI) of the irregular micro specimens and to avoid the influence of rigid body rotation and machine elastic deformation, an optical device is used to measure the deformation in the ROI by an optical flow technique (digital image correlation, DIC). Instead of using the local displacement of a two-point extensometer as in conventional uniaxial tensile experiments, a 4-point-frame optical extensometer is introduced to measure tension stretch in both vertical and horizontal directions to obtain an average macro measurement in the reference frame. The same 4-point-frame measurement is applied to numerical simulations for comparison with the experiments as shown in Fig.3.

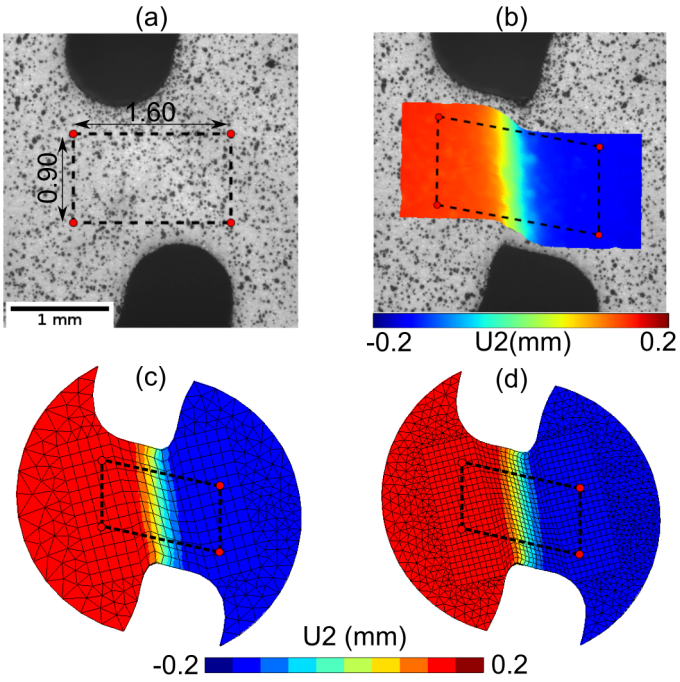

Figure 3: 4-point-frame optical extensometer on (a) reference and (b) deformed images for image correlation. The same 4-point-frame is chosen from finite element model to compare experiment with the simulations of (c) coarse and (d) fine meshes at the same deformed step under SO loading. The shown displacement field in (b) was calculated by software VIC2D.

Briefly speaking, a symmetric right stretch tensor $\mathbf{U}$ can be computed from the displacement of 4 points. Two components, tension stretch U_{11} and the absolute value of shear stretch U_{12}, are chosen as the tension and shear local measurements respectively. More details of measurement definition and experiments can be checked in Kong et al. [2023a].

3.2. Model calibration strategy

A hybrid experimental-numerical model calibration procedure is used to identify all parameters including plasticity parameters and damage parameters. Firstly, plasticity parameters including texture parameters, slip system hardening parameters and localization parameters were calibrated with the pseudo-experimental database from the macroscopic non-damage Bron-Besson (BB) model. It is a Barlat-type model with a phenomenological yield function to represent the plastic anisotropy [Bron and Besson, 2004]. The anisotropy is represented by 12 parameters in the two fourth order

symmetric tensors, and 4 other parameters controlling the shape of the yield surface uniformly. The parameters of BB model were calibrated with the experimental database using single element calculations for uniaxial tension tests (L, T and D) and full meshed calculations for the notched tensile tests (L and T) as well as the shear test (L) in Kong et al. [2023a]. A good agreement was obtained between experiments and macroscopic BB simulations with the optimized parameters. Theoretically, the microscopic polycrystalline model (PC) could be calibrated in the same way but it is much more time-consuming for full meshed calculations during parameter optimization, especially since the large number of parameters (43) requires several thousand iterations for the convergence of the calibration. In addition, BB model is able to generate pseudo-experiments for database augmentation under various stress states (e.g., simple shear and non-proportional loadings with a single element, for which the same boundary conditions are applied on both models). Secondly, the CRL damage model parameters R_0, Q_0 and c_0 were identified with fracture experiments of the micro specimens under proportional shear and tension loadings. As mentioned earlier, the porous plasticity parameters are the ones calibrated in Rousselier [2021] for the same aluminum alloy. Lastly, the optimized model is used to predict the behavior under different non-proportional load path changes (i.e., ST and TS).

The measured Young's modulus $E = 74$ GPa and Poisson's ratio $\nu = 0.33$ are assumed as constant in the material identification. The viscosity parameters in Eq.8 are set as $n_s = 20$, $K_s = 25$ MPa $s^{-1/n}$ corresponding to very small viscous stress.

Step I: Plasticity parameters calibration using simple simulations with macroscopic Bron-Besson model. It is noted that the CRL and void damage models were not activated since the plasticity was calibrated with the non-damage macroscopic plasticity model at this step.

- **Texture parameters (11):** For an orthotropic texture with 3 components, Euler angles of 12 grains are represented with 3 groups (j=1,2,3) including each volume fraction $frac_j$. The 4 grains in each group are symmetrically distributed as [ϕ_1^j, Φ^j, ϕ_2^j, $frac_j$], [-ϕ_1^j, Φ^j, -ϕ_2^j, $frac_j$], [-ϕ_1^j, -Φ^j, -ϕ_2^j, $frac_j$], [ϕ_1^j, -Φ^j, ϕ_2^j, $frac_j$]. In total, 11 texture variables were identified (4×3 except $frac^1$=0.25-$frac^2$-$frac^3$).

- **Slip system hardening parameters (22):** 7 isotropic hardening parameters including R and three groups (i=1,2,3) of non-linear isotropic hardening parameters Q^i, b^i in Eq.10, three groups of latent hardening parameters (h_2^i to h_6^i, i = 1,2,3), assuming $h_1^i = 1$.

- **Localization parameters (10) for the self-consistent homogenization scheme:** The fourth order $\underline{\underline{D}}$ was proposed by Sai et al. [2006] for anisotropic materials. With the Voigt notation, $\underline{\underline{D}}$ has 10 independent components (D_{11}, D_{21}, D_{22}, D_{23}, D_{31}, D_{32}, D_{33}, D_{44}, D_{55}, D_{66}) for orthotropic materials. The scalar modulus C of initial elastic accommodation is set to 20 000 MPa as in [Rousselier et al., 2009].

Step II: Damage parameters calibration using 3D mesh calculations with fracture experimental database.

- **Damage parameters (2):** Three parameters R_0, Q_0 in Eq.15 and c_0 in Eq.14 were calibrated with the proportional experimental database (shear-only and tension-only tests) in terms of global nominal stress - stretch curves, at the first abrupt load drop deciding for the stretch to fracture as crack initiation. It could be assumed that $Q_0 = -R_0$ for a complete softening. b_0 is set as 2 for a slow decrease of the critical stress, resulting in stress softening and strain localization [Rousselier and Luo, 2014, Rousselier, 2021].

3.3. Plasticity calibration

All calculations have been performed with the commercial finite element software Z-set [Besson and Foerch, 1997, Zset]. During step I for plasticity calibration, there are two types of calculations. First, Z-set simulator performed point simulations with a given material model by controlling strain or stress components (e.g. ε_{11} or σ_{11}) without any finite element. Secondly, simple calculations including uniaxial tensile and simple shear were applied on a single hexahedral element (c3d8). The calibration weight of each comparison is set differently.

Based on the optimized parameters, Fig.4 presents a good agreement between simulations with the non-damage macroscopic model (Bron-Besson, noted as BB) and polycrystalline model (PC). It is noted that the hardening capacity of BB model is completely saturated after the pre-shear loading ($\varepsilon_{12} = 0.10$) in (e) non-proportional loading.

The calibrated results with the $1 \times 1 \times 1\ mm^3$ single element calculations are shown in Fig.4 (f)(g) for uniaxial tensile and (h) for simple shear tests. A moderate anisotropy is shown in (f) but the Lankford ratio is smaller than 0.5. A good agreement between Lankford coefficients is shown in Fig.4 (f). The curves of both models are close. A smooth wave is found from simple shear displacement $U_2 = 0.4$ mm for PC model in Fig.4 (h), which came mainly from a quick hardening saturation of group one (large parameter b_1) with a late hardening of group two (small b_2).

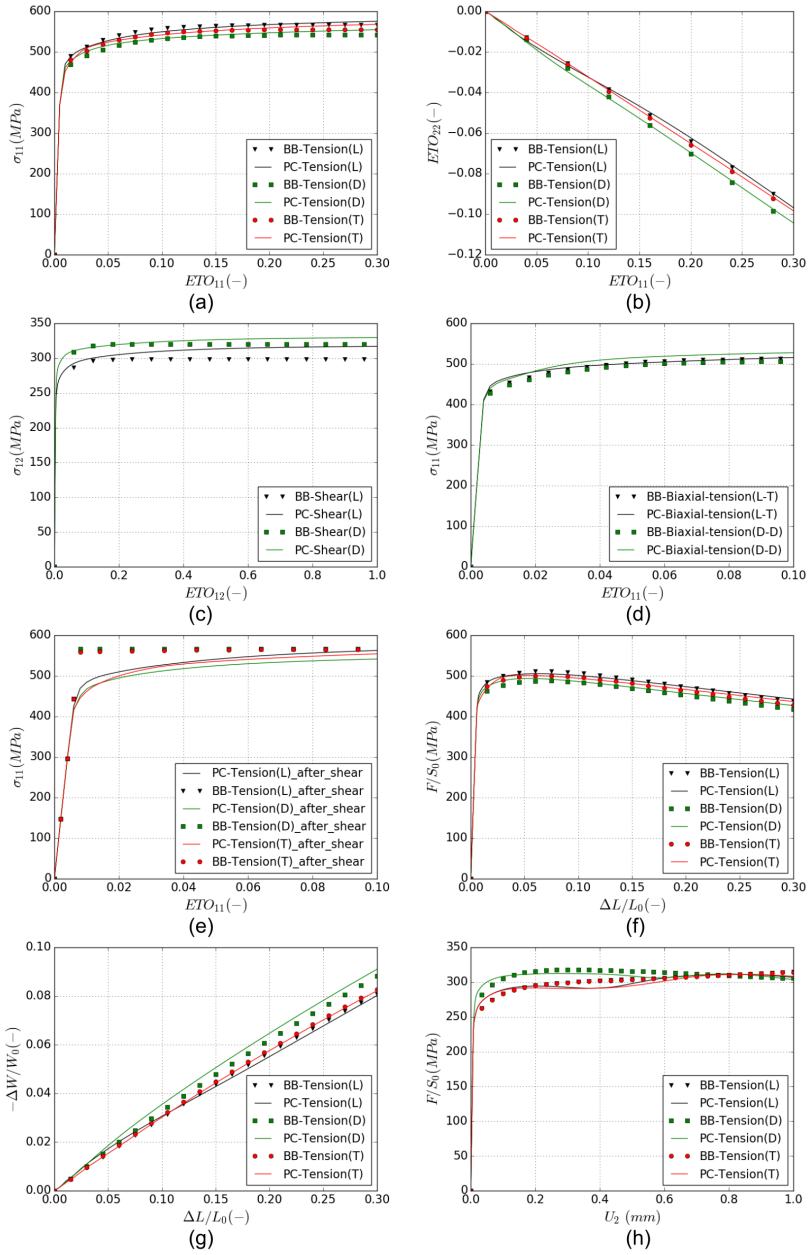

Figure 4: Plasticity calibration using macroscopic (no damage) Bron-Besson model: simulations in terms of (a) tensile stress versus strain and (b) tensile lateral strain versus strain, (c) shear stress, (d) bi-axial tensile stress, (e) shear followed by tensile loading conditions. Single element calculations in (f)(g) uniaxial tensile loading and (h) simple shear loading conditions. ETO_{11} and ETO_{12} are components from total strain matrix, while ΔL and ΔW stand for length change in loading and transverse directions, U_2 for simple shear displacement in the single element calculation.

The optimized texture parameters are given in Tab.2. The EBSD pole figures in the form of stereographic projections are represented by the three colored dots in comparison to the experimental EBSD poles in Fig.5. Although the aim of the reduced texture is to model mechanical behavior rather than to fit exactly the experimental texture, there is no apparent contradiction between the model and real textures; the *free of pole* zones are similar.

index j	$\phi_1^j(^\circ)$	$\Phi^j(^\circ)$	$\phi_2^j(^\circ)$	$frac_j$(-)
1	17.812	51.563	-21.263	0.0930
2	56.636	18.943	-24.991	0.0790
3	-125.082	152.494	- 0.247	0.0781

Table 2: Optimized texture parameters including Euler angles and volume fractions for a reduced orthotropic texture with 12 grains, where three groups (i.e., j = 1, 2, 3) are represented in different colors in Fig.5 with four symmetric orientations each.

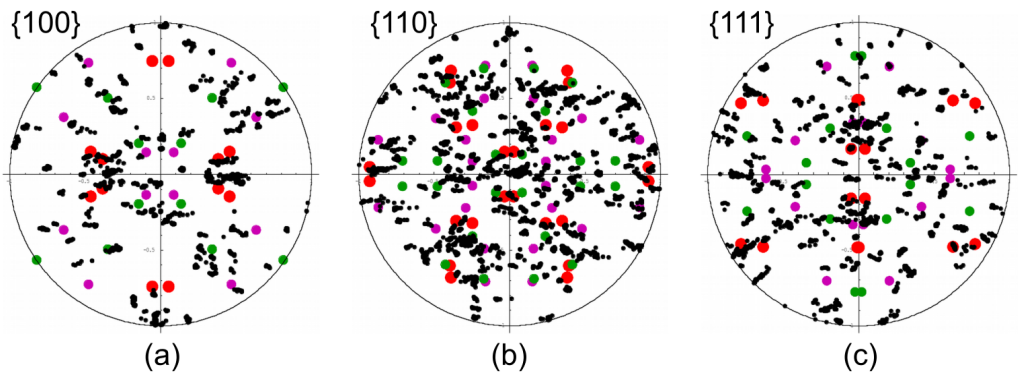

Figure 5: EBSD pole figures for full-thickness specimen (small black dots) and reduced texture (colored dots): (a) {100}, (b) {110} and (c) {111} poles.

The other calibrated parameters are given in Tab.3 for the slip system hardening parameters and in Tab.4 for localization parameters. Note that the latent hardening parameters h_4^1=1.587 and h_4^2=4.381 are very large when calibrated with non-proportional loading. In Rousselier [2021], the larger value was h_2^1=0.197 for the same material.

	Young's modulus E (MPa)		Poisson's ratio ν		R (MPa)	
	74 000		0.3		181.371	
index	Q^i	b^i	h_2^i	h_3^i	h_4^i	h_5^i	h_6^i
1	35.642	21.461	4.777e-3	1.525e-3	1.587	1.132e-1	3.831e-2
2	10.062	2.287	6.142e-2	1.149e-2	4.381	1.060e-5	2.293e-5
3	14.228	1.000	1.122e-1	2.694e-2	3.139e-1	2.704e-2	1.466e-1

Table 3: Optimized parameters for slip system hardening.

D_{11}	D_{12}^*	D_{13}^*	D_{21}	D_{22}	D_{23}
1.311e3	1.050e3	1.088e3	7.759e2	1.027e3	5.885e2
D_{31}	D_{32}	D_{33}	D_{44}	D_{55}	D_{66}
2.367e1	3.405e1	4.345e2	2.480e2	1.398e1	8.218e3

Table 4: Optimized localization parameters for the self-consistent homogenization scheme, where D_{12}^* and D_{13}^* are not calibrated but calculated from Eq.B.2.

4. Application to ductile damage in non-proportional load

During the step II for damage calibration, the cross-shaped specimen in Fig.2 (c) is meshed with hexahedral elements in the central region (c3d8) and triangular prism elements (c3d6) elsewhere as shown in Fig.6. The central region mesh is Cartesian as in previous works (A sharp notched *Kahn* specimen in Rousselier [2021] for tear testing of thin aluminum alloy products, similar to the well-known compact-tension (CT) specimen). The crack is expected to propagate more or less in the mesh direction. The use of similar meshes should optimize the transferability from one geometry to another with the same damage parameters. In fact, the mesh is Cartesian in the two rectangular blocks to the left and right of the minimum section (Fig.6). Two different mesh sizes in ROI are applied and denoted as coarse and fine meshes respectively (Fig.6 (b)(d) and (c)(e) respectively), in order to investigate the mesh size effect on strain localization and crack propagation. In the minimum section, the mesh is slightly curved to model the curvature of the notches. In the center of the specimen, the size is $w_0/12 = 116.67$ μm and $w_0/24 = 58.33$ μm respectively. The two meshes are denoted "100 μm" and "50 μm". In these two meshes, the total element numbers are 21 776 and 70 816, whereas the hexahedral elements (c3d8) are 1 728 and 13 056. There are 8 and 16 elements in the thickness direction, respectively. In order to save computation time, only Cartesian mesh at the region of interest (ROI) is modeled with the polycrystalline model in red, while the element set of non-ROI sample is modeled with the macroscopic Bron-Besson model in grey and the four supporters as isotropic elastic steel with high Young's modulus ($E = 210$ GPa) in blue.

In full meshed calculations, a Gauss point (or integration point) is considered as *broken* state when the combined damage variable d defined in Eq.16 reaches 1. Once the half of Gauss points within a single element are *broken* (e.g. 4 *broken* points in a hexahedral element c3d8), the damaged element is totally removed including all Gauss points inside.

4.1. Damage calibration

As mentioned at the end of Section 2, the porous plasticity parameters are the ones in [Rousselier, 2021] for the same aluminum alloy. In order to calibrate the shear damage parameters, simulations using full 3D meshes with different element sizes were carried out in proportional load paths including shear-only (SO) and tension-only (TO). The two meshes described above (in the figures: coarse mesh 100 μm curves in red and fine mesh 50 μm curves in blue) are used for the mesh dependency study of the polycrystalline model. Besides, the results of the macroscopic BB

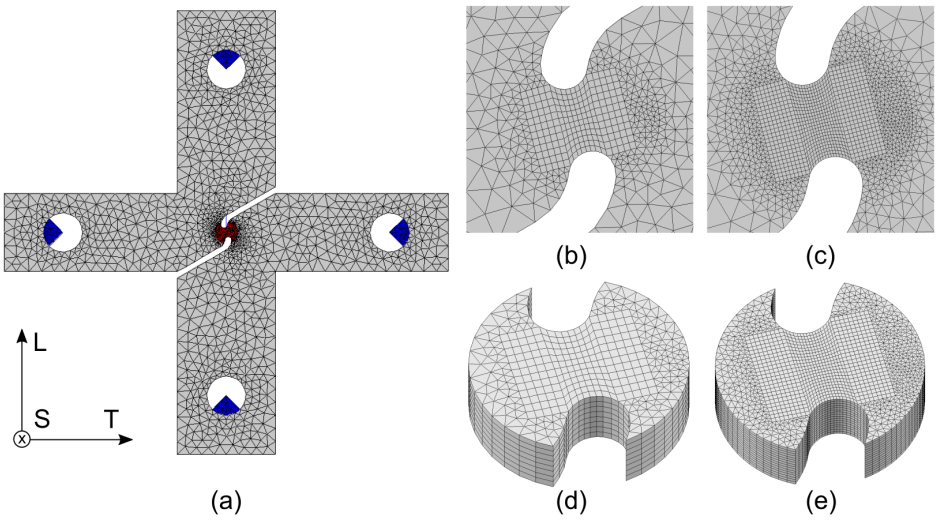

Figure 6: (a) Full size of mesh geometry and the region of interest (ROI) in (b)(d) coarse mesh and (c)(e) fine mesh.

model are included for the comparison. The calibration procedure is based on the response from coarse mesh, and the experimental ductility scatter is shown with a representative experimental database for each loading [Kong et al., 2023a].

375 The global curves in terms of the nominal stress versus shear or tension stretch exhibit the critical points within the experimental ductility scatters in grey in Fig.7 for (a)(b) SO and (c)(d) TO. The two damage variables were optimized as R_0=$-Q_0$=283 MPa, c_0=0.08.

In Fig.7 (a)(b), numerical curves fit well with the experimental one till crack initiation (CI) under shear loading (SO). They start to become more or less unstable with oscillations after the 380 first force drop at $U_{12} = 0.135$ illustrated in (b). Small load drops occur, due to element removal. The point of the first load drop is considered as the CI point to compare with the experimental failure (analyzed in Kong [2022]). In the next section, the local fields are investigated at the time of CI point. Moreover, the predictive failure occurs slightly earlier in the fine mesh calculation. The load decrease, related to the crack growth rate, is larger with the fine mesh (Fig.7 (a)(b)).

385 Fig.7 (c)(d) shows the smooth load-stretch curves under proportional tension load (TO). Numerically, crack initiation occurs when the slope decreases critically as seen in (d). The sample was totally *broken* (force drop to zero) at $U_{11} = 1.115$, which is in the range of the experimental ductility scatter, for the coarse mesh group. The removed elements on the section indicate the

macroscopic fracture path. The fine mesh group failed earlier around $U_{11} = 1.095$. The two critical points are illustrated as fracture (F) points in (d). Note that the coarse mesh size corresponds to *Kahn* specimen mesh size in Rousselier [2021], the load-crack mouth opening curve is also in agreement with the experimental curve.

Mesh size has a limited effect on the crack initiation under shear loading but a larger effect under tension loading.

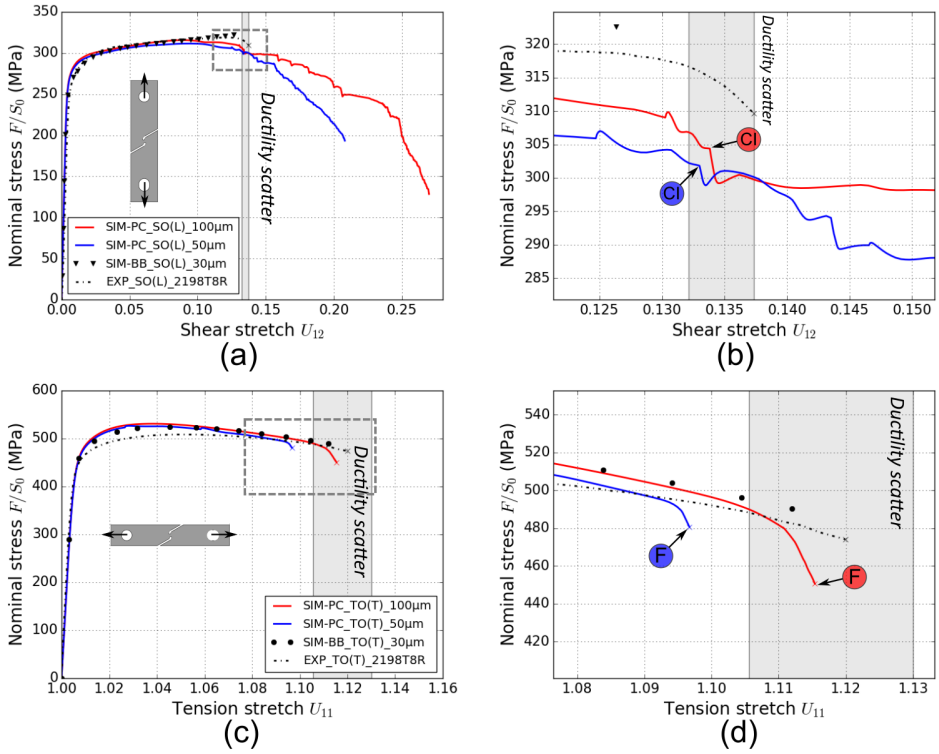

Figure 7: Damage parameters calibration in comparison with experimental data: The curves in terms of nominal stress versus shear or tension stretch under proportional loading paths of (a) shear-only (SO) and (c) tension-only (TO). The detailed regions near crack initiation are zoomed in (b) for SO and (d) for TO. The experimental ductility scatters under monotonic loadings (SO and TO) are presented in grey box. BB and PC in the legend stand for Bron-Besson and polycrystalline models respectively.

4.2. Model prediction and validation under non-proportional load paths

The polycrystalline model with the optimized plasticity and damage parameters is used to predict non-proportional load paths 'shear to tension' (ST) and 'tension to shear' (TS). It should be noticed that the non-proportional loading is not biaxial. The sample was loaded under the first loading direction and then unloaded, subsequently it was re-loaded under the second loading direction till fracture.

Fig.8 presents the curves in terms of nominal stress versus shear or tension stretch at (a) shear and (b) tension periods of non-proportional 'shear to tension' (ST) load path. Experimentally, the specimen was loaded under shear till $U_{12} = 0.081$ and then unloaded as illustrated in (a); subsequently, the specimen was loaded horizontally under tension till fracture in (b) as a black dashed line. Polycrystalline simulations using meshes of two different element sizes perfectly match the experiments during the shear pre-loading. They also have a good agreement with the experimental stress level and initial tension stretch of the subsequent tension loading, better than the results of the macroscopic non-damage model. As in Fig.4 (e), the BB model gives good maximum stress (black dots) but its hardening capacity is almost saturated by the first loading in shear. The difference between both models could be related to the non-diagonal parameters of the hardening matrices. The curves of tension loading show a smooth force decrease due to damage softening in Fig.8 (b) as seen under the proportional loading TO. Crack initiation occurs in the elbows and it is close to fracture points. However, due to the effect of shear pre-loading, there is an obvious ductility reduction and stress cross hardening compared to the proportional loading TO [Kong et al., 2023a]. The tension stretch from coarse mesh in red broke at $U_{11} = 1.085$ while the one from fine mesh in blue failed a bit earlier at $U_{11} = 1.065$. The ductility prediction of coarse mesh as failure stretch U_{11}^f is in the experimental scatter range from 1.084 to 1.106 illustrated in (b) as blue block. In summary, the polycrystalline model succeeded in predicting plasticity and ductility during the non-proportional load path 'shear to tension' (ST). Two specific steps are chosen to observe the local fields in the next section: the end of shear pre-loading (SE) and tension fracture point (F).

The results of the other load path change 'tension to shear' (TS) are exhibited in Fig.8 for (c) tension and (d) shear periods. The specimen was loaded under tension till U11=1.060 and then unloaded as shown in (c); The deformed sample was subsequently loaded under shear till fracture in (d). The end of tension pre-loading (TE) and shear crack initiation (CI) are selected as two specific steps for the local field observation in TS.

In the second shear loading (Fig.8 (d)), PC simulations show a good prediction in terms of shear stretch shift and macroscopic stress with the results of the macroscopic model (BB). Although the predictive maximal stress of PC model is 4% less than the experiment, it is close to that of BB model (triangle symbols) since PC model was calibrated with BB model. As discussed in Kong et al. [2023a], a nominal stress (F/S_0) decrease seen in the second shear loading compared to proportional shear (SO), is mainly due to the thickness reduction (cross-section reduction $S < S_0$) during pre-tension loading. This is consistent with the experimental data and has been checked in FE simulations. Thus quantitatively, the stress reduction sensitively depends on the pre-tension loading. Experimentally, although the average stretch at CI (U_{12}^{CI-TS}) is similar to the value of the proportional test SO ($U_{12}^{CI-SO} = 0.135$), the stretch at CI of TS shows a large scatter (from 0.117 to 0.157) in the blue block of Fig.8 (d). The ductility reduction also highly depends on the extent of pre-tension loading [Kong et al., 2023a]. Numerically, before crack initiation, the coarse mesh calculation (red) presents a relatively stable nominal stress level as SO while the calculation with fine mesh (blue) gives a smooth drop in the shear loading curve (Fig.8 (d)). Crack initiated at U_{12} = 0.152 for coarse mesh and 0.105 for fine mesh. The CI point of coarse mesh is in the range of the experimental scatter. After crack initiation during shear shown in (d), the nominal stress level of the coarse mesh (in red) slightly decreased or even maintained for a short distance before each force drop due to element removal. On the contrary, the nominal stress of the fine mesh (in blue) decreased smoothly and rapidly after the CI point.

In tension loadings (TO and ST), the global curves drop smoothly before fracture as shown in Fig.7 (d) and Fig.8) (b). Strain and damage localized near two notches. The Gauss points (or integration points) were *broken* in localized elements and the elements were removed. The rest elements in the band would be damaged, broken and removed before next converge. There was a critical load decrease when crack initiates and before fracture. Crack initiation (CI) points are very close to fracture (F) points. Finally, the whole *broken* ligament completely lost force capability and a force drop to zero was seen in the global curve. Therefore, the fracture point of TO/ST is easy to choose in simulation as experiment. While in the simulations under shear loadings (SO and TS), the specimen still has force capability after the first set of element removal. The global curves continue to maintain for a while with a small force drop after each element removal in Fig.7 (a) and Fig.8 (d). Hence, we define the first load drop as 'crack initiation' (CI) point for SO and TS instead of fracture points. Experimentally, the load history might not be continuously captured

and a pop-in is triggered after a critical drop [Petit et al., 2018], where they studied the effect of different machine stiffness on the force instability before fracture.

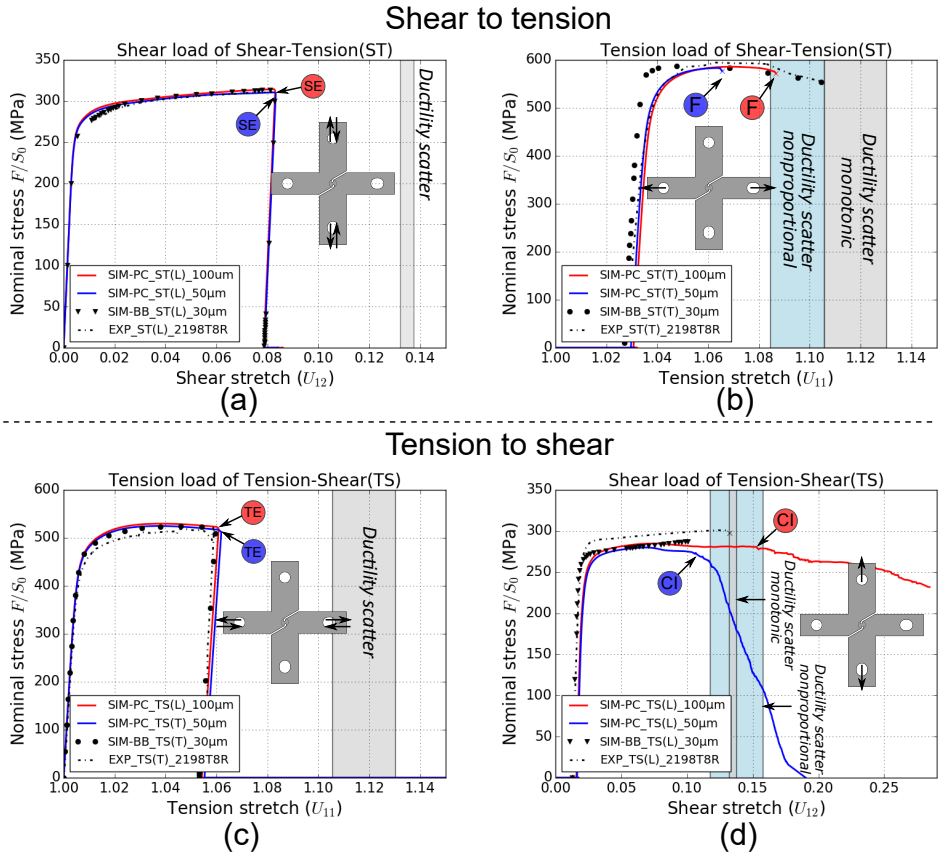

Figure 8: Predictions of the calibrated polycrystallline model under non-proportional load path changes: (a) shear and (b) tension loading periods in 'shear to tension' (ST) as well as (c) tension and (d) shear loading periods in 'tension to shear' (TS). The experimental ductility scatters are shown in in grey box for monotonic loadings (SO and TO) and blue box for non-proportional loadings (ST and TS). BB and PC in the legend stand for Bron-Besson and polycrystalline models respectively.

4.3. Local fields

460 The polycrystalline model with the optimized parameters was compared to experiments in terms of global stress versus stretch curves. Different fields at crack initiation (CI) or fracture (F) point under proportional and non-proportional loading paths are presented in Fig.9 for cumulative strain, Fig.10 for porosity and Fig.11 for maximal Coulomb slip respectively.

4.3.1. Cumulative strain fields

Fig.9 presents the cumulative strain fields in (a)-(d) obtained by the 3D FE simulations in comparison to experimental results by surface DIC before fracture in (e)-(h) as well as the final fracture paths in (i)-(l) under four different loading paths.

Shear-only (SO): A similar band in terms of shape and amplitude is generated in the highly deformed region at the surface in Fig.9 for both (a) numerical simulation and (e) experimental measurement at the CI point. The crack path in (i) superposed well with the strain field before fracture. The strain distribution stayed homogeneous through the thick direction (S) from the surface to the middle plane according to the numerical calculation. The maximal value reached up to 0.93 for the coarse mesh and 1.00 for the fine mesh, while a maximal strain could reach 1.10 experimentally measured from the sample surface in (e).

Tension-only (TO): Fig.9 exhibits the cumulative strain fields of the surface at the step before fracture from (b) simulation and (f) experimental DIC under tension-only loading, in which a wider strain band is shown. As in a notched tensile specimen, the strain was localized at notches. Although the strain level was only around 0.40 at the surface, the maximal strain could reach up to 0.69 and 0.67 in the mid-thick plane as known from the simulations of coarse and fine meshes respectively. It is noteworthy that two fracture points were differently chosen for each calculation as shown in Fig.7 (d), where the calculation with fine mesh *broke* earlier at U_{11}^F=1.095 than that with coarse mesh (U_{11}^F=1.115). The simulated fracture path also corresponds to the red dashed line in Fig.9 (j), which links both notch regions with the elevated strain.

'Shear to tension' (ST): For the predictive non-proportional 'shear to tension' load path, Fig.9 shows the cumulative strain field on the specimen surface between (c) simulation and (g) experiment at the tension fracture point after pre-shear loading. Compared to the strain field under proportional shear only (SO), the strain band was obviously widened under subsequent tension loading. At the precedent loading point of shear end (SE) shown in Fig.8 (a), where shear stretch U_{12} as 0.081, the strain field is similar to the one under SO state with a maximal value of 0.56 for the coarse mesh (0.60 for fine mesh). At the succeeding tension fracture point, maximal strain in the mid-thick plane increased to 0.74 and 0.70 obtained by both calculations of coarse and fine

meshes respectively. Although there is a ductility reduction (26%) in terms of tension stretch to fracture U_{11} under ST (U_{11}^{F-ST}=1.085) compared to proportional TO (U_{11}^{F-TO}=1.115), the cumulative strain to fracture slightly increased (ε_{cum}^{ST}=0.74 versus ε_{cum}^{TO}=0.69 for coarse mesh; ε_{cum}^{ST}=0.70 versus ε_{cum}^{TO}=0.67 for fine mesh) under non-proportional load path ST. Moreover, the strain band indicates the fracture path in (k) as well.

'Tension to shear' (TS): For the other non-proportional 'tension to shear' load path, the cumulative strain field at the CI point is shown in Fig.9 for (d) simulation and (h) experiment. The strain field of TS test was highly localized up to a magnitude of 0.8 in the direction parallel to vertical shear load. As numerical result showed, unlike the homogeneous strain field along the thickness direction under proportional SO, the maximal strain under TS was situated in the middle thick plane due to the pre-tension straining. The cumulative strain elevated to 0.28 (0.36 for fine mesh) at the point of pre-loading tension end (TE), subsequently strain expanded to 0.97 (0.81 for fine mesh) when applied to shear loading, which is close to the value (0.93 and 1.00 for coarse and fine mesh respectively) under proportional SO. The fracture path is consistently led by the cumulative strain field under TS in Fig.9 (l).

In summary, under different loading paths including proportional (SO, TO) as well as non-proportional (ST, TS), the cumulative strain fields, obtained by experiments and numerical simulations, agree well in harmony in terms of field shape and amplitude, at least on the specimen surface. Furthermore, the strain location predictively reveals the potential fracture path at each loading condition.

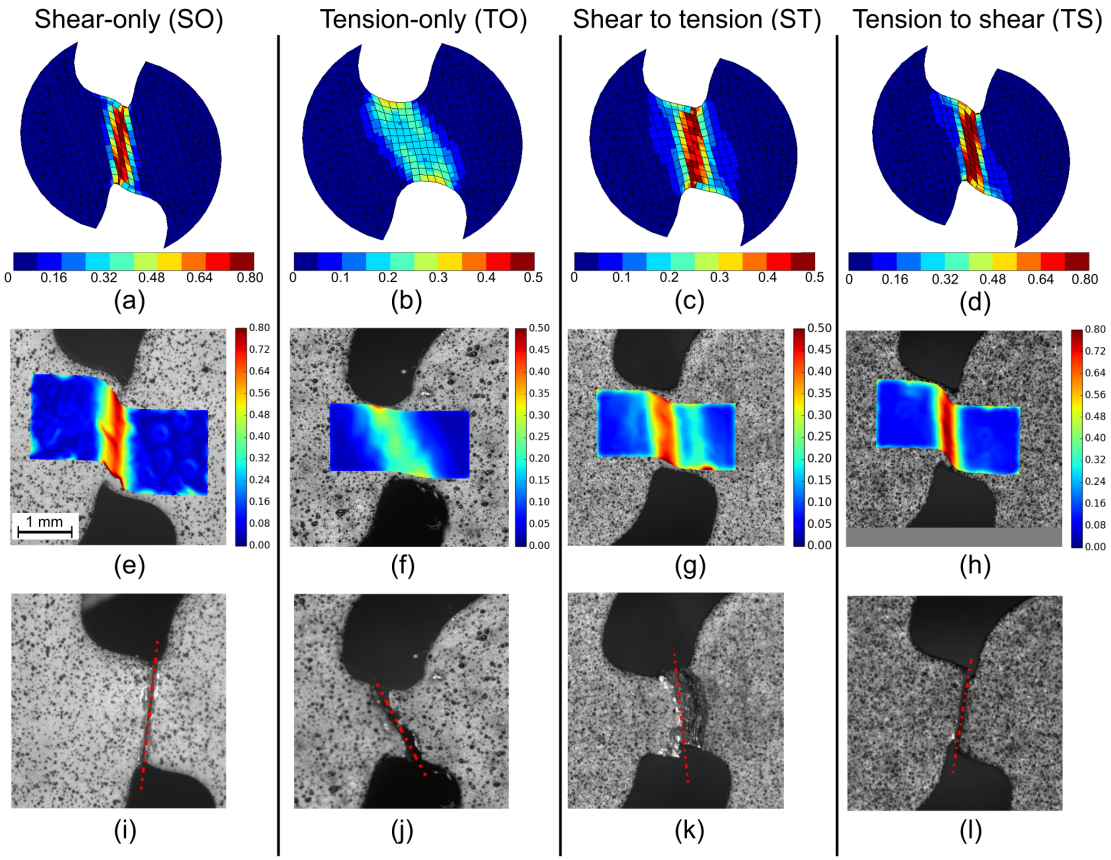

Figure 9: (a-d) Simulated cumulative equivalent strain fields on the surface at last time before fracture with comparison to (e-h) experimental results, as well as (i-l) fracture paths under different load paths: shear-only (SO), tension-only (TO), 'shear to tension' (ST) and 'tension to shear' (TS).

4.3.2. Porosity fields

As one of the major damage variables, the coarse mesh fields of porosity f at the mid-thick plane are shown in Fig.10 at each critical time under different load paths.

Shear-only (SO): Although the porosity has a relatively low level around 2% when damage initiated in Fig.10 (a), considering that the initial porosity f_0 was set as 0.01%, the porosity significantly increased under shear loading and was located homogeneously in the entire strain band. It might be due to the fact that the region is not perfectly under simple shear state but mixed with the tensile component ($U_{11} \neq 1$) as discussed in the previous subsection.

Tension-only (TO): As the cumulative strain field in Fig.9 (b), the porosity localized in the same region in the middle thickness plane on notches as shown in Fig.10 (b). Porosity achieved a large level of more than 6%, which stands for the classic void growth driven by tension-dominated high stress triaxiality. From the fractography observations in Kong et al. [2023a], damage features including intermetallic particle broke and matrix-particle debonding were found under TO, which resulted in large dimples.

'Shear to tension' (ST): Fig 10 presents the porosity fields under non-proportional loading from (c) shear to (d) tension loading. At the end of shear pre-loading (U_{12}=0.08), at around 60% of shear stretch at crack initiation under SO ($U_{12}^{CI-SO} = 0.135$), the porosity was homogeneously localized on the band with the value as 0.9%. Subsequently, the region expanded under the second tension loading at fracture point, where the maximal porosity value doubled to 1.8%. The porosity level at failure under ST was solely one-third of the one (6.1%) under proportional TO, but the field is much more homogeneous. The fields and maximal values obtained by the calculation of fine mesh are close to the ones of coarse mesh.

'Tension to shear' (TS): The porosity fields under load path changes are presented in Fig.10 from (e) tension to (f) shear. At the end of pre-tension loading ($U_{11} = 1.06$) in (e), which is around half of proportional tension stretch to fracture ($U_{11}^{F-TO} = 1.115$), the porosity localized at the same region as the one under TO and grew to 0.8% (1.1% for fine mesh). When sample was turned to the shear loading till crack initiation, the porosity was filled up homogeneously in the entire ligament with a nearly threefold increase as 2.4% (2.7% for fine mesh). The maximal value is located at the center region away from the notches as shown in Fig.10 (f).

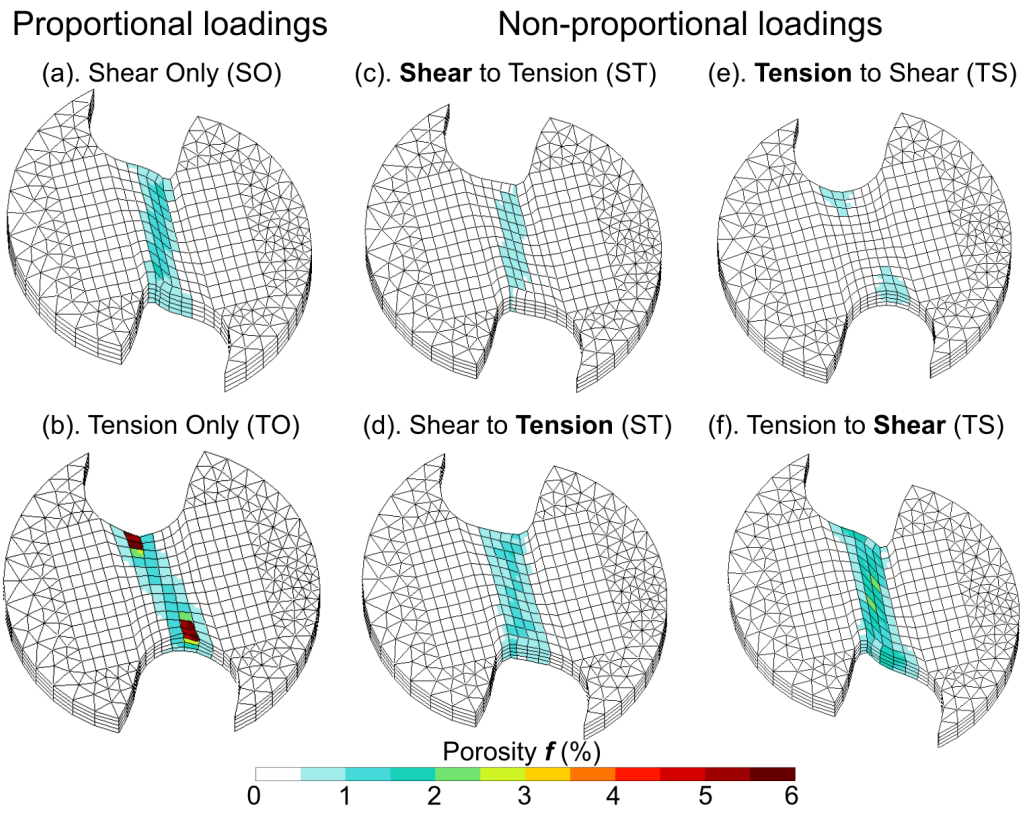

Figure 10: The predicted porosity fields at the mid thickness plane (z=0.5 mm) under different load paths: (a) Shear only (SO), (b) Tension only (TO), (c-d) 'Shear to tension' (ST) and (e-f) 'Tension to shear' (TS) at the critical points as CI or F. Here (c), (e) are the first loadings and (d), (f) are the second loadings under two non-proportional loadings respectively.

4.3.3. Maximal Coulomb slip fields

Fig.11 presents the fields of maximal Coulomb slip γ^C_{max} out of 144 slip systems γ^C_s $(s = 1-144)$ as well as the broken fields under four load paths. Although γ^C_{max} ranges from 0 to 3 ($\gamma_u = 3$), the legend range in Figure is set from 0 to 1 since the damage effect is already large. There are two colors dark red and yellow in broken fields, which represent the *broken* and *deleted* states respectively.

Shear-only (SO): Several elements with activated Coulomb slip are seen around the band border at the time of crack initiation (CI) point in Fig.11 (a). The elements, whose Coulomb slip value is greater than 0.1 at least one Gauss point, are selected to represent damage in Fig.11 (b)(c). The

activated slips were not situated on the shear band but 100 μm away from the central line through the entire thickness. Moreover, some other fully activated Coulomb slips were also found on the notch edges, where the stress is mainly under a compression state. Fig.11 (d) presents the broken field of selected elements at the same time, where the damaged region was mainly due to the fully activated Coulomb slips.

Tension-only (TO): Fig.11 (e) exhibits maximal Coulomb slip at fracture point under tension-only (TO) loading. At the slip system scale, Coulomb slips were only activated in the region of strain localization, as the cumulative strain and porosity. The total 20 elements, with a maximal Coulomb slip greater than 0.1, are selected to represent the damage region in (f)(g). Most of them were at the notch edge region with maximal strain and porosity, which showed a consistent localization under TO at the middle thickness plane of the broken field in (h). Damage is likely to originate from the region and propagate along the band as experimentally observed.

'Shear to tension' (ST): For the non-proportional ST loading, the maximal Coulomb slip field is shown in Fig.11 (i) at the fracture point of the second tension loading. The location was at the mid-thickness plane and 200μm away from the notches. At the end of shear pre-loading, the damaging effect was limited and the slip value was less than 0.1. The slips grew larger under the subsequent tension loading but showed a different location from the one under proportional TO in Fig.11 (e). The elements with maximal Coulomb slip greater than 0.1 are selected and shown in (j)(k). The elements with low values were found at notches while the ones with high values were located at the mid-thickness plane as indicated by *broken* field in (l).

'Tension to shear' (TS): Fig 11 (m) presents the maximal Coulomb field at shear CI point under another load path change from 'tension to shear' (TS). At the point of pre-tension end (TE), there was hardly an activated slip. The effect of tension pre-loading ($U_{11} = 1.06$) seems very limited in terms of Coulomb slip. The selected elements as shown in (n)(o) indicate that the activated slips were located at the band border similar to proportional SO. The broken field in (p) agrees well with the distribution of fully activated Coulomb slips.

The pre-tension extent ($U_{11} = 1.06$) probably is not enough to bring any damaging effect and thus more simulations with different pre-tension levels will be discussed in the next section.

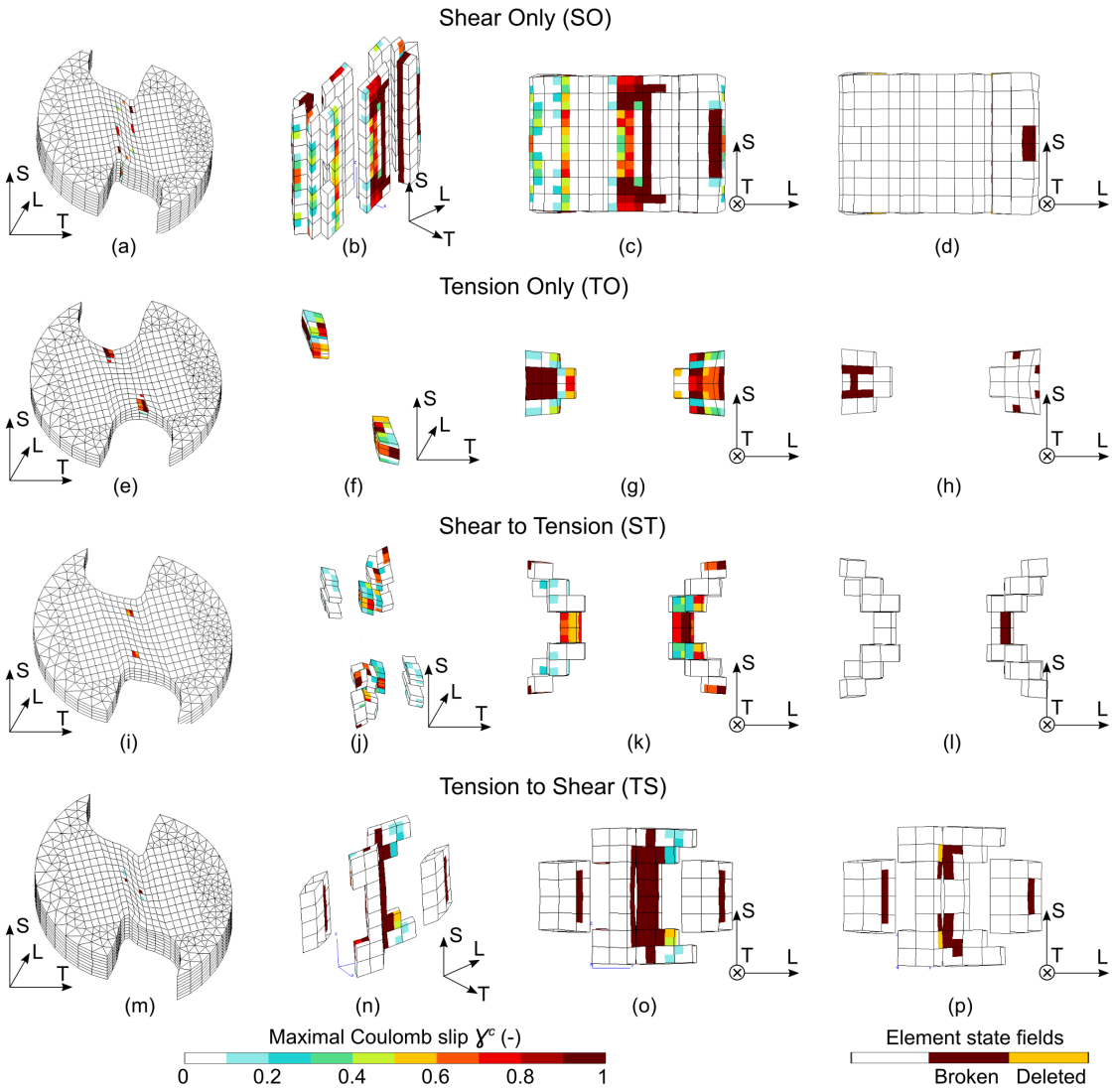

Figure 11: Maximal Coulomb slip fields under different load paths: (a-c) shear only (SO), (e-g) tension only (TO), (i-k) 'shear to tension' (ST) and (m-o) 'tension to shear' (TS), where (a)(m) are full thickness mesh and (e)(i) half-thickness mesh. (d)(h)(l)(p) Broken fields under each load path at the critical points as CI or F.

The maximal values of cumulative strain, porosity, and maximal Coulomb slip of the coarse and fine meshes under the different loading paths above are concluded in Tab.5. Both coarse and fine mesh calculations exhibit similar field distributions in the ROI. The fine mesh calculations show

590 smoother fields and larger maximal values of damage than the coarse mesh calculations.

100 μm	ε_{cum}	f (%)	γ^C_{max}	50 μm	ε_{cum}	f (%)	γ^C_{max}
SO	0.93	1.8	3	SO	1.00	2.1	3
TO	0.69	6.1	3	TO	0.67	6.2	3
ST-s	0.56	0.9	0.075	ST-s	0.60	0.9	0.49
ST-t	0.74	1.8	3	ST-t	0.70	1.7	3
TS-t	0.28	0.8	0	TS-t	0.36	1.1	0
TS-s	0.97	2.4	3	TS-s	0.81	2.7	3

Table 5: Maximal cumulative strain ε_{cum}, porosity f and maximal Coulomb slip γ^C_{max} under different loadings including proportional SO, TO as well as non-proportional ST, TS for coarse (left) and fine (right) meshes. ST-s means shear end (SE) point, ST-t for CI point, TS-t for tension end (TE) point, and TS-s for CI point.

5. Discussion

5.1. Experimental comparison under ST

An *in situ* laminographic experiment under non-proportional load 'shear to tension' (ST) was carried out at ID19 at the European Synchrotron Radiation Facility (ESRF) and described in detail in Kong et al. [2022]. On the macro scale, the effect of pre-shear loading on ductility resulted in a 20% reduction of the tension stretch to fracture compared to the proportional tension loading. On the micro scale, two main types of damage features, intermetallic particle cracks and flat cracks, were found. Damage nucleation has already been observed at the end of shear pre-loading at nearly zero stress triaxiality. The nucleated damage grew and led to the final fracture during tensile loading after shear pre-loading.

Compared to the physical observations via 3D laminography, the predictive combined damage fields of the polycrystalline model under ST load path changes included the classic particle-related damage (i.e., porosity) and the transgranular flat cracks (i.e., activated Coulomb slips) at the slip system scale. It is not easy to describe the complex geometry of 3D damage fields, either measured or simulated. The comparison of damage location between experimental observation and numerical prediction is presented in Fig.12. Experimentally, damage was quantified as the projected *surface void fraction* in the experiment [Kong et al., 2022]. The segmented damage in yellow sub-volume ($792\times1152\times720$ μm^3) in (a) is visualized in (b)(f) L-T top view and (c)(g) L-S side view at pre-shear end (b-c) and tension before fracture (f-g) loadings. Numerically, the combined damage fields are shown for the coarse mesh simulation at the two same loading steps: (d) shear end and (h) tension fracture. It is worth noting that the maximum value of combined damage was projected along the T orientation to the L-S cross section in (e)(i), in order to compare with experimental segmentation in (c)(g). Although a Gauss point is considered as *broken* state when the combined damage variable is d=1, the useful damage range is merely set from 0 to 0.12 in the fields. This last value may seem small for a totally *broken* state, but in fact the softening is already large. Physically, a void volume fraction equal to 0.12 is a large value in metallic alloys. In experiments from Kong et al. [2022], the damage quantified as surface void fraction reached around 0.1 just before failure.

At the end of pre-shear loading, damage nucleated in the band region through all thickness in Fig.12 (c). The *surface void fraction* is 0.01 and it is in good agreement with the numerical

simulation where combined damage is homogeneously distributed around 0.02 through the thickness (S) shown in (e). When it turned to the subsequent tensile loading, nucleated damage in shear continued to grow and coalesced to macroscopic fracture in the strain band in (f) from the last scan under tension before failure, where several flat cracks were found and distributed in the yellow sub-volume in (g). The combined damage obtained from numerical calculation continued to grow as well to more than 0.10 (close to experimental quantification of *surface void fraction*) in the middle-thickness plane shown in (i). Furthermore, the damage localization is at 0.2 mm from the notch edge in the mid-thickness plane, which could be linked to the observed damage near the middle thickness plane in (g). Although the observed damage is irregular and not symmetrical, this metallurgical variability cannot be captured in the simulation. In summary, the model managed to indicate not only the damage location under shear but also damage growth quantitatively under subsequent tension loading during the non-proportional load path.

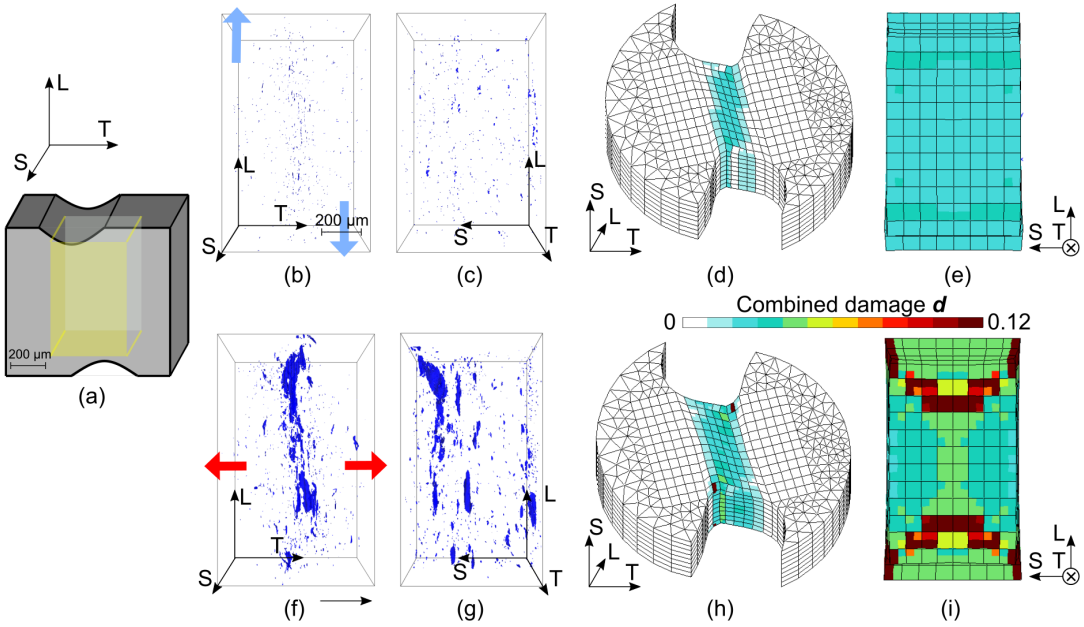

Figure 12: Damage visualization of yellow sub-volume (a) via 3D laminography at (b)(c) the end of pre-shear loading and (f)(g) the end of subsequent tension loading before fracture. Combined predicted damage fields of damaged element at (d)(e) end of pre-shear loading and (h)(i) end of subsequent tension loading for coarse mesh.

5.2. Prediction on effect of different pre-loading

In this study, only one type of experiment, where the sample was pre-loaded to the half of stretch to fracture of the proportional test, was conducted. Brünig et al. [2021] investigated the effect of 45%, 65% and 90% shear pre-loading on the followed tension loading as well as the effect of 50%, 75% and 85% tension preloading on the followed shear loading respectively. A remarkable displacement reduction was found due to pre-straining. The higher the pre-straining is, the more the ductility reduces. However, the mechanism behind the reduction under load path change was not clearly identified by fractography.

In order to quantitatively investigate the effect of different pre-loadings, virtual experiments with the optimized polycrystalline model using 100 μm mesh have been carried out to predict the plastic behaviors and find out the origin of pre-loading effects under two non-proportional loadings ST and TS respectively.

5.2.1. 'Shear to tension' (ST)

Non-proportional 'shear to tension' (ST) loadings with different shear pre-loadings ranging from U_{12}=0.03 to 0.12 (22% to 89% of shear crack initiation point U_{12}^{DI-SO}=0.135) are presented in Fig.13 (a) for pre-shear loading period and (b) for subsequent tension loading period. Overall, it shows that the greater pre-shear loading, the smaller the tension stretch to fracture using fracture (F) points as Fig.8 (b). The plasticity shear hardening resulted in a higher stress level except for the last three simulations, whose failures occurred even before the maximum load that could be obtained without damage, probably due to large shear damage. The initial tension stretch shift, as there is a slight tension stretch during shear pre-loading, was found larger with increasing pre-shear straining. If the initial tension stretch shift during pre-shear is not considered, which means all specimens were assumed to be virgin, the ductility reduction would be even higher as shown in Fig.13 (c). Interestingly, the short pre-shear loading simulation ($U_{12} = 0.03$ in dark blue) failed even later than the monotonic group in black. All the fracture points from both original and shifted curves are shown in Fig.13 (d) in terms of tension stretch to fracture versus pre-shear stretch, including the experimental ductility scatters from SO and ST of U_{12}=0.08 as grey and blue boxes respectively. There is a linear tendency of ductility reduction with increasing pre-shear stretch except for the exceedingly damaged tests. Although the crystalline model is sensitive to the resolved shear stress of each slip system, three groups of U_{12}=0.07, 0.08 and 0.09 pre-loadings

under similar global stress levels present different tension stretches to fracture. It indicates that the ductility reduction is not global stress level dependent. Experimentally it already showed that
665 shear-dominated loading led to damage nucleation and growth even at zero stress triaxiality. The origin of ductility reduction under non-proportional loading from 'shear to tension' is likely related to the induced shear damage, quantitatively in porosity and maximal Coulomb slips.

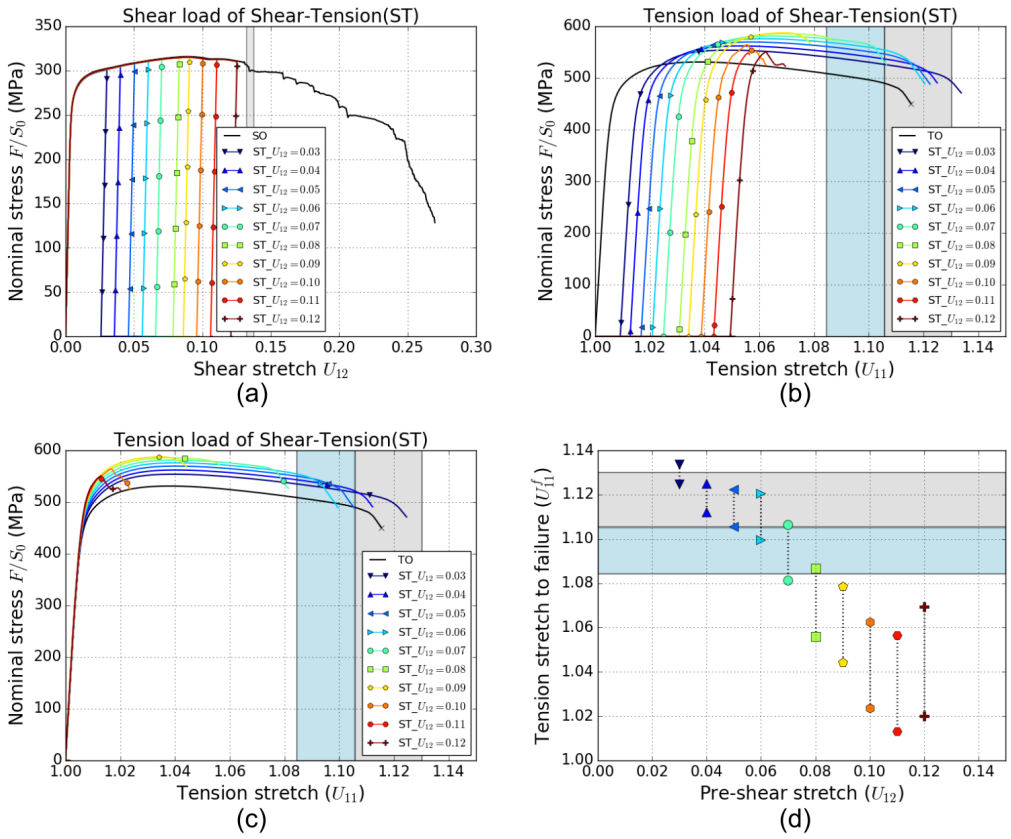

Figure 13: The predicted curves in terms of nominal stress versus shear or tension stretch under non-proportional 'shear to tension' (ST) in (a) pre-shear loading and (b) subsequent tension loading. (c) The shifted curves under tension loading assuming pre-strained specimens as virgin. (d) The summary of tension stretch to fracture points from original and shifted groups with regard to pre-shear stretch. The grey box represents the monotonic experimental scatter while the blue one stands for the experimental scatter of tension tests after U_{12}=0.08 pre-shear stretch.

5.2.2. 'Tension to shear' (TS)

Fig.14 presents the results under another non-proportional loading 'tension to shear' (TS) with different tension pre-loadings U_{11}=1.05 to 1.11 (43% to 95% of monotonic tension stretch to fracture point U_{11}^{f-TO} =1.115) at periods of (a) tension loading and (b) shear loading. With increasing the tension pre-loading, the shear stress softening was larger mainly due to thickness reduction during tension. Force dropped slowly with oscillations in the shear curves. As in shear loadings (SO and TS), the first crucial force drop point is defined as crack initiation (CI) point. CI points are used in Fig.14 (b) as in Fig.8 (d) while fracture (F) points cannot be used because large tension pre-loading simulations give no critical *fracture* point. Fig.14 (c) presents the shifted shear curves with neglecting the tension pre-loading effect. Despite the crack initiated earlier from the large pre-loading groups (U_{11} = 1.09, 1.10 and 1.11) compared to the monotonic shear-only group, the reduction of ductility did not appear for other pre-tension groups. All shear stretch at the CI points from both original and shifted curves are summarized in Fig.14 (d), including the experimental scatters of monotonic SO and TS with U_{11}=1.05 and 1.06 as grey and blue boxes respectively. The effect of pre-tension loading on the shear stretch at DI is less clear from the predictive TS simulations with different pre-loading extent, and a large experimental scatter (the blue box in Fig.14) is also found in the TS experiments even with the same extent of pre-loading. As presented in the discussion of Kong et al. [2023a], the strain distribution in the shear band depends on the extent of pre-tension, and the latter influences the deformed extent of the ligament geometry between two notches. Brünig et al. [2021] found a strong scatter (from 0% to 47%) as well for 'tension to shear' load path changes using an H-shaped sample. In local fields of TS, no Coulomb slip activated and only small porosity value is found on the notch edges at the end of pre-tension (U_{11}=1.06). The effect of a low pre-tension level (U_{11} <1.10) is negligible on the crack initiation points.

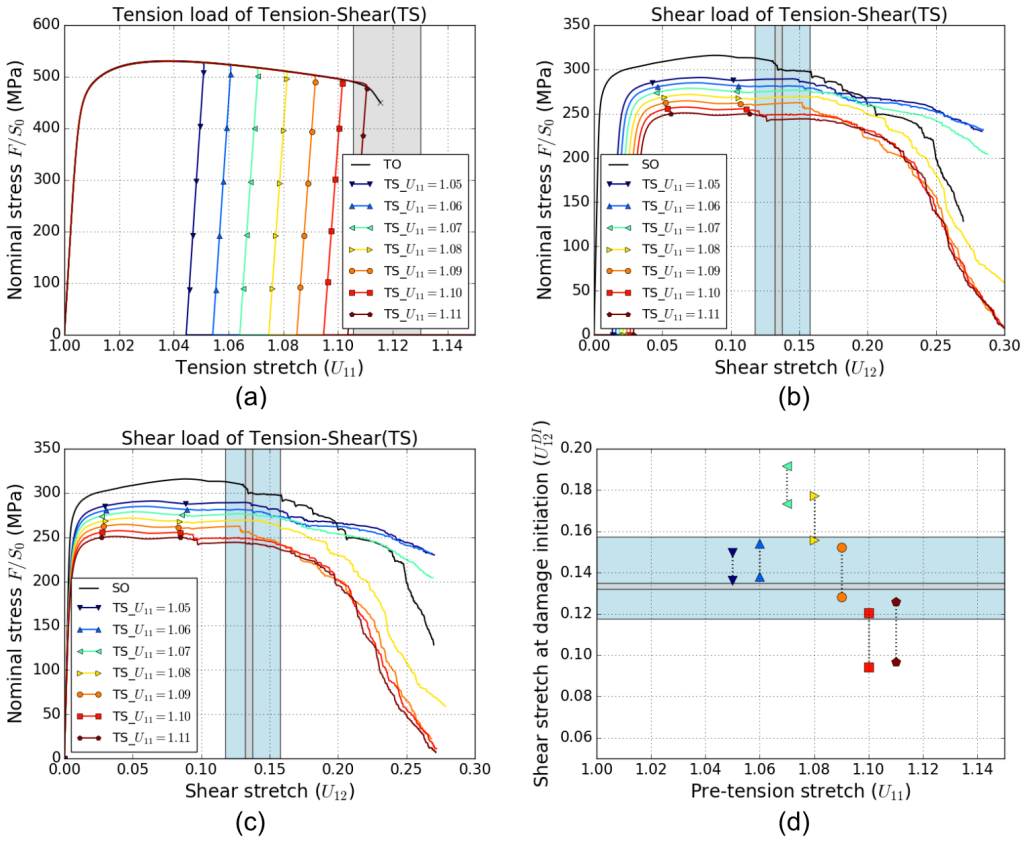

Figure 14: The predicted curves in terms of nominal stress versus shear or tension stretch under non-proportional 'tension to shear' (TS) in (a) pre-tension loading and (b) subsequent shear loading. (c) The shifted curves under shear loading assuming pre-strained specimens as virgin. (d) The summary of shear stretch at crack initiation from original and shifted groups with regard to pre-tension stretch. The grey box represents the monotonic experimental scatter while the blue one stands for the experimental scatter of shear tests after U_{11}=1.05-1.06 pre-tension stretch.

6. Conclusion

According to two damage mechanisms (i) initiation, growth and coalescence of micrometric voids and (ii) a grain-related smooth and flat fracture feature in Al-Cu-Li 2198-T8 alloy, the first mechanism is classically modeled with macroscopic porous plasticity. The second mechanism takes place at the grain scale and could be related to transgranular slip bands. The Coulomb-Rousselier-Luo (CRL) model at the slip system scale is used for this second ductile fracture mechanism. The mean-field polycrystalline framework is used to combine porous plasticity and the CRL model. Polycrystalline plasticity with interaction matrices between slip systems is also necessary to model the non-proportional load paths because the activated slip systems are not the same in tension and in shear.

A Reduced Texture Methodology (RTM) was used to provide computational efficiency and this approach involved a large reduction in the number of representative crystallographic orientations (12-grain model using 12 crystallographic orientations, 144 slip systems). The reduced texture parameters (Euler angles, volume fractions) were calibrated from mechanical tests only, simultaneously with the plasticity model parameters, using single element calculations under proportional tension, shear and non-proportional 'shear to tension' (ST) loadings. A few latent hardening parameters are very large when calibrated with non-proportional loading. The experimental texture is not used for the calibration. A good agreement between experimental and model curves was obtained for all loading conditions. Although the aim of the reduced texture is to model mechanical behavior rather than to fit exactly the experimental texture, there is no apparent contradiction between the reduced and real textures.

The porous plasticity parameters are those of Rousselier [2021] for the same aluminum alloy. In order to calibrate the two CRL model parameters, simulations using full 3D "coarse 100 μm" meshes were performed in proportional load paths including shear-only (SO) and tension-only (TO). The curves in terms of nominal stress versus shear or tension stretch are compared. With the calibrated damage parameters, damage initiation takes place in the experimental ductility scatter bands of both loadings. The comparison with the "fine 50 μm" meshes shows the classical mesh size dependence in tension. In shear, the damage initiation point is less dependent on the mesh size but the post initiation load drop is less regular and more mesh-size dependent than in tension. The Cartesian mesh is probably less suitable for the propagation of shear cracks that are not exactly in the direction of the mesh. Regularization methods that could limit the mesh dependence are

beyond the scope of the present work.

In non-proportional 'tension to shear' (TS) and 'shear to tension' (ST) load paths, experimental and simulated curves are in good agreement up to the points of damage initiation. In ST, the hardening capacity is not saturated by the first tension load that does not activate the same slip systems as the shear load. The macroscopic plasticity model used for comparison saturates rapidly at the maximum load. In TS, this effect is less significant but still present. The predicted damage initiation points fall in the experimental ductility scatter bands of both non-proportional loadings. In TS, the post initiation load drop related to crack propagation is again more mesh-size dependent than in tension loadings.

For all loadings, the cumulative equivalent strain fields on the surface of the samples agree well with the experimentally measured fields. In the volume between the two notches of the specimen, the experimental damage was visualized as the projected surface void fraction in the short and transverse directions. In the case of 'shear to tension' (ST), it has been compared to the quadratic combination of simulated void and shear damage (void volume fraction and maximum Coulomb slip). The location of damage initiation under shear but also damage growth under subsequent tension loading during the non-proportional load path are similar in the experiment and simulation, although the spatial definition is much coarser in the latter.

An interesting contribution of numerical simulation is the possibility to perform more virtual experiments under non-proportional loadings to explore the effect of pre-loading on ductility reduction. The combined damage+stress hardening/softening and geometrical softening (thickness reduction) from pre-loading are believed to affect the stretch to fracture. In ST, the ductility is reduced in function of the pre-shear stretch. In TS, only a large pre-tension stretch has a significant effect on ductility.

Appendix A. Finite strain formulation

It is assumed that $\vec{X}$ and $\vec{x}$ are the positions of material points in the initial configuration and in the actual configuration respectively. $\underline{F}$ is the deformation gradient, $\underline{L}$ is the velocity gradient, $\underline{D}$ is the Eulerian strain rate and $\underline{W}$ is the rotation rate:

$$\underline{F} = \frac{\partial \vec{x}}{\partial \vec{X}},\ \underline{L} = \dot{\underline{F}} \cdot \underline{F}^{-1},\ \underline{D} = \frac{1}{2}(\underline{L} + \underline{L}^T),\ \underline{W} = \frac{1}{2}(\underline{L} - \underline{L}^T) \tag{A.1}$$

The integrated rotation tensor $\underline{Q}$ is calculated from:

$$\dot{\underline{Q}} \cdot \underline{Q}^{-T} = \underline{W},\ \underline{Q} = \underline{Q}(0) \text{ at } t = 0. \tag{A.2}$$

$\underline{Q}(0) \neq \underline{1}$ defines the initial orientation of the material frame for an anisotropic material.

The objective material embedded frame is the so-called co-rotational frame associated with the rotation tensor $\underline{Q}$ [Ladévèze, 1980, Yoon et al., 1999a,b, Hoc and Forest, 2001, Rousselier and Luo, 2014]. The transportation of the deformation rate and Cauchy stress tensors ($\underline{D}$, $\underline{S}$) in the current space frame to the co-rotational frame give the tensors ($\underline{E}$; $\underline{\Sigma}$):

$$\dot{\underline{E}} = \underline{Q}^T \cdot \underline{D} \cdot \underline{Q},\ \underline{\Sigma} = \underline{Q}^T \cdot \underline{S} \cdot \underline{Q} \tag{A.3}$$

Appendix B. The fourth order tensor $\underline{\underline{D}}$

With Voigt notations, the form of the fourth order tensor $\underline{\underline{D}}$ for orthotropic materials is:

$$\underline{\underline{D}} = \begin{pmatrix} D_{11} & D_{12} & D_{13} & 0 & 0 & 0 \\ D_{21} & D_{22} & D_{23} & 0 & 0 & 0 \\ D_{31} & D_{32} & D_{33} & 0 & 0 & 0 \\ 0 & 0 & 0 & D_{44} & 0 & 0 \\ 0 & 0 & 0 & 0 & D_{55} & 0 \\ 0 & 0 & 0 & 0 & 0 & D_{66} \end{pmatrix} \tag{B.1}$$

The tensor $\underline{\underline{D}}$ has the symmetries in D_{ijkl}=D_{jikl}=D_{jilk}=D_{ijlk}, but it has not the strong symmetry in D_{ijkl}=D_{klij}. As $\underline{\underline{D}}$ is a linear relation between two deviatoric tensors, 7 independent components are needed from the relation:

$$D_{11} + D_{21} + D_{31} = D_{12} + D_{22} + D_{32} = D_{13} + D_{23} + D_{33} \tag{B.2}$$

In total, there are 10 independent coefficients (including three D_{44},D_{55} and D_{66}). Since D_{12} and D_{13} are not considered as variables in the optimization but calculated from Eq.B.2, the parameters in $\underline{\underline{D}}$ are optimized as followed:

$$\underline{\underline{D}} = \begin{pmatrix} 1311 & 1050^* & 1088^* & 0 & 0 & 0 \\ 775.9 & 1027 & 588.5 & 0 & 0 & 0 \\ 23.67 & 34.05 & 434.5 & 0 & 0 & 0 \\ 0 & 0 & 0 & 248.0 & 0 & 0 \\ 0 & 0 & 0 & 0 & 13.98 & 0 \\ 0 & 0 & 0 & 0 & 0 & 8218 \end{pmatrix} \tag{B.3}$$

Appendix C. The hardening matrix H_{st}

The hardening matrix H_{st} has a crucial role in physical phenomena like cross-hardening and additional hardening in non-proportional loadings. The 12×12 symmetric hardening matrix H_{st} expresses the interaction among 12 slip systems corresponding to each slip direction for the FCC crystallographic structure and it can be denoted with different 3×3 matrices in Eq.C.2 and Eq.C.3:

$$H_{st} = \begin{bmatrix} H & H_{12} & H_{13} & H_{14} \\ H_{12}^T & H & H_{23} & H_{24} \\ H_{13}^T & H_{23}^T & H & H_{34} \\ H_{14}^T & H_{24}^T & H_{34}^T & H \end{bmatrix} \tag{C.1}$$

$$H = \begin{bmatrix} h_1 & h_2 & h_2 \\ h_2 & h_1 & h_2 \\ h_2 & h_2 & h_1 \end{bmatrix}, H_{12} = \begin{bmatrix} h_4 & h_5 & h_5 \\ h_5 & h_3 & h_6 \\ h_5 & h_6 & h_3 \end{bmatrix}, H_{13} = \begin{bmatrix} h_5 & h_6 & h_3 \\ h_4 & h_5 & h_5 \\ h_5 & h_3 & h_6 \end{bmatrix} \tag{C.2}$$

$$H_{14} = \begin{bmatrix} h_5 & h_3 & h_6 \\ h_5 & h_6 & h_3 \\ h_4 & h_5 & h_5 \end{bmatrix}, H_{23} = H_{24}^T = H_{34} = \begin{bmatrix} h_6 & h_5 & h_3 \\ h_3 & h_5 & h_6 \\ h_5 & h_4 & h_5 \end{bmatrix} \tag{C.3}$$

Each 12×12 symmetric hardening matrix H_{st}^i in Eq.C.1 only depends on six parameters h_1 to h_6 where h_1=1 for the diagonal terms according to Table 2 of Méric et al. [1991]. The optimized coefficients are not unique, because three groups under the same form are considered with different parameters for each group.

Appendix D. Texture evolution

During intense shear loading, there is very large deformation (i.e. cumulative strain reaches nearly 1) at the localization band. The underlying mechanism such as crystallographic texture evolution can be taken into account in this condition, see for example in Rousselier et al. [2009].

Texture evolution is modeled by actualizing the lattice orientation ($\vec{n}_s$,$\vec{l}_s$). In the material co-rotational frame, the rotation rate vanishes:

$$\underline{W}^c = 0 \tag{D.1}$$

Classically to model texture evolution, an assumption is taken that all grains have the same total rotation rate as Taylor-like hypothesis:

$$\underline{\omega}_g = \underline{\omega}_g^e + \underline{\omega}_g^p \equiv \underline{W}^c = 0, \ \forall g = 1, N. \tag{D.2}$$

The plastic rotation rate of each grain is:

$$\underline{\omega}_g^p = \sum_{s=1}^{M} \underline{q}_{sg} \dot{\gamma}_{sg} \tag{D.3}$$

where $\underline{q}_{sg}$ stands for the rotation tensor of each slip system s within the grain g:

$$\underline{q}_{sg} = (\vec{l}_{sg} \otimes \vec{n}_{sg} - \vec{n}_{sg} \otimes \vec{l}_{sg})/2 \tag{D.4}$$

The lattice rotation tensor $\underline{R}_g$ of each grain in the co-rotational frame can be obtained from:

$$\dot{\underline{R}}_g \underline{R}_g^T = \underline{\omega}_g^e = -\underline{\omega}_g^p = -\sum_{s=1}^{M} \underline{q}_{sg} \dot{\gamma}_{sg} \tag{D.5}$$

The slip systems of the actualized texture are defined by:

$$\vec{n}_{gs} = \underline{R}_g \vec{n}_{gs}(0), \vec{l}_{gs} = \underline{R}_g \vec{l}_{gs}(0) \tag{D.6}$$

It is assumed that $\underline{\omega}_g^e$ is constant during every small time increment Δt, thus Eq.D.5 can be integrated the following:

$$\underline{R}_g(t + \Delta t) = \exp(\underline{A}).\underline{R}_g(t) \tag{D.7}$$

where $\underline{A} = \underline{\omega}_g^e \Delta t$.

According to Cayley-Hamilton's theorem in Eq.D.8 for the particular form of $\underline{A}$, the development of $exp(\underline{A})$ is limited to the three terms $\underline{A}^0 = \underline{1}$, $\underline{A}^1$ and $\underline{A}^2$:

$$\underline{A}^3 = -w^2 \underline{A},\ w^2 = A_{12}^2 + A_{23}^2 + A_{31}^2 \tag{D.8}$$

$$\exp(\underline{A}) = \underline{1} + (1 - \frac{w^2}{6} + ...)\underline{A} + (\frac{1}{2} - \frac{w^2}{24} + ...)\underline{A}^2 \tag{D.9}$$

Eq.D.9 is applied in the numerical integration, with a sufficiently large number of terms. The close-form equation is the following:

$$\exp(\underline{A}) = \underline{1} + \frac{\sin w}{w}\underline{A} + \frac{1 - \cos w}{w^2}\underline{A}^2 \tag{D.10}$$

Once texture evolution option is activated in the model, all the parameters need to be optimized again for the calibration strategy. Limited to time for the re-calibration work with texture evolution, a trial calculation with current optimized parameters was launched in order to verify the effect of texture evolution. It is highly reminded that all parameters were calibrated without texture evolution, which means the new trial calculation does NOT fit with experiment in terms of nominal stress versus stretch.

Fig.D.15 presents (a) maximal Coulomb slips field at damage initiation point, including (b)(c) the selected element with slip values greater than 0.1. Unlike the field without texture evolution

in Fig.11 (a-c), the Coulomb slips were activated mainly on the localization band instead of band borders. It indicates the region where the granular related flat cracks were found. This difference demonstrates the apparent effect of texture evolution on the highly deformed region under intense shear loading.

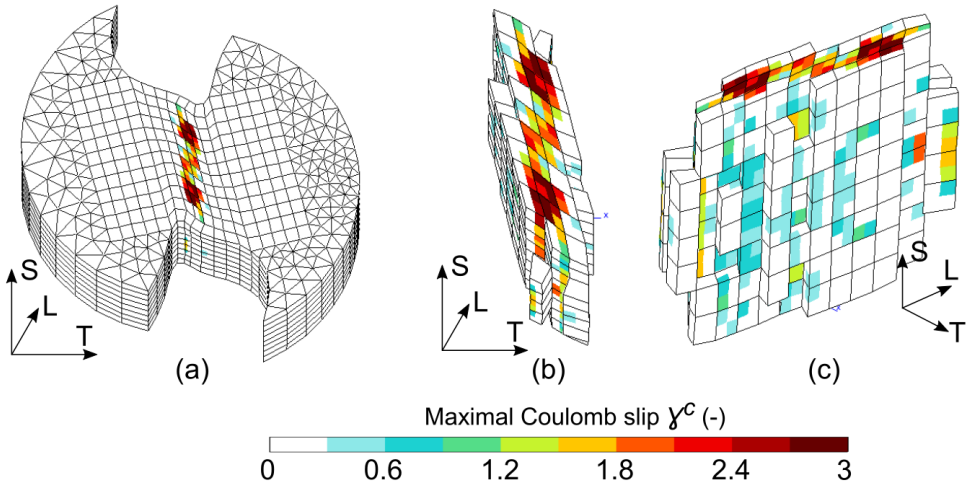

Figure D.15: Maximal Coulomb slip field under proportional shear-only (SO) with using texture evolution.

The re-calibration procedure is necessarily performed with activating option of texture evolution in the next step. The methodology in this paper could be applied again with optimized parameters using texture evolution.

Authorship contributions

Category 1

Conception and design of study: G. Rousselier, T. F. Morgeneyer

Acquisition of data: X. Kong, D. Missoum-Benziane

Analysis and/or interpretation of data: X. Kong, D. Missoum-Benziane, G. Rousselier, T. F. Morgeneyer

Category 2

Drafting the manuscript: X. Kong

Revising the manuscript critically for important intellectual content: G. Rousselier, T. F. Morgeneyer

Category 3

Approval of the version of the manuscript to be published (the names of all authors must be listed):
X. Kong, D. Missoum-Benziane, G. Rousselier, T. F. Morgeneyer

Declaration of Competing Interest

The authors declare that they have no known competing financial interests or personal relationships that could have appeared to influence the work reported in this paper.

Acknowledge

The financial support of Agence Nationale de la Recherche (ANR-LAMBDA project: 17-CE08-0051) is gratefully acknowledged.

References

Mohamed Achouri, Guenael Germain, Philippe Dal Santo, and Delphine Saidane. Experimental characterization and numerical modeling of micromechanical damage under different stress states. *Materials & Design*, 50:207–222, 2013. ISSN 0261-3069. doi: https://doi.org/10.1016/j.matdes.2013.02.075. URL https://www.sciencedirect.com/science/article/pii/S0261306913001866.

Yuanli Bai and Tomasz Wierzbicki. A new model of metal plasticity and fracture with pressure and lode dependence. *International Journal of Plasticity*, 24(6):1071–1096, 2008. ISSN 0749-6419. doi: https://doi.org/10.1016/j.ijplas.2007.09.004. URL https://www.sciencedirect.com/science/article/pii/S0749641907001246.

Yingbin Bao and Tomasz Wierzbicki. On fracture locus in the equivalent strain and stress triaxiality space. *International Journal of Mechanical Sciences*, 46(1):81–98, 2004. ISSN 0020-7403. doi: https://doi.org/10.1016/j.ijmecsci.2004.02.006. URL https://www.sciencedirect.com/science/article/pii/S0020740304000360.

Frédéric Barlat, Daniel J. Lege, and John C. Brem. A six-component yield function for anisotropic materials. *International Journal of Plasticity*, 7(7):693–712, 1991. ISSN 0749-6419. doi: https://doi.org/10.1016/0749-6419(91)90052-Z. URL https://www.sciencedirect.com/science/article/pii/074964199190052Z.

Imad Barsoum and Jonas Faleskog. Rupture mechanisms in combined tension and shear—experiments. *International Journal of Solids and Structures*, 44(6):1768–1786, 2007. ISSN 0020-7683. doi: https://doi.org/10.1016/j.ijsolstr.2006.09.031. URL https://www.sciencedirect.com/science/article/pii/S0020768306003921. Physics and Mechanics of Advanced Materials.

J. Besson and R. Foerch. Large scale object-oriented finite element code design. *Computer Methods in Applied Mechanics and Engineering*, 142(1):165 – 187, 1997. ISSN 0045-7825.

F. Bron and J. Besson. A yield function for anisotropic materials application to aluminum alloys. *International Journal of Plasticity*, 20(4):937–963, 2004. ISSN 0749-6419.

Michael Brünig, Moritz Zistl, and Steffen Gerke. Numerical analysis of experiments on damage and fracture behavior of differently preloaded aluminum alloy specimens. *Metals*, 11(3), 2021. ISSN 2075-4701.

Michael Brünig, Steffen Gerke, and Vanessa Hagenbrock. Stress-state-dependence of damage strain rate tensors caused by growth and coalescence of micro-defects. *International Journal of Plasticity*, 63:49–63, 2014. ISSN 0749-6419. doi: https://doi.org/10.1016/j.ijplas.2014.04.007. URL https://www.sciencedirect.com/science/article/pii/S0749641914000904. Deformation Tensors in Material Modeling in Honor of Prof. Otto T. Bruhns.

Ante Buljac, Xiang Kong, Lukas Helfen, François Hild, and Thilo F. Morgeneyer. Shear loading dominated damage mechanisms and strain localization studied by in situ 3d laminography imaging and digital volume correlation for aa2198-t8. *Mechanics of Materials*, 178: 104558, 2023. ISSN 0167-6636. doi: https://doi.org/10.1016/j.mechmat.2023.104558. URL https://www.sciencedirect.com/science/article/pii/S0167663623000042.

Clément Cadet, Jacques Besson, Sylvain Flouriot, Samuel Forest, Pierre Kerfriden, and Victor de Rancourt. Ductile fracture of materials with randomly distributed voids. *International Journal of Fracture*, 230(1):193–223, Jul 2021. ISSN 1573-2673. doi: 10.1007/s10704-021-00562-7. URL https://doi.org/10.1007/s10704-021-00562-7.

Clément Cadet, Jacques Besson, Sylvain Flouriot, Samuel Forest, Pierre Kerfriden, Laurent Lacourt, and Victor de Rancourt. Strain localization analysis in materials containing randomly distributed voids: Competition between extension and shear failure modes. *Journal of the Mechanics and Physics of Solids*, 166:104933, 2022. ISSN 0022-5096. doi: https://doi.org/10.1016/j.jmps.2022.104933. URL https://www.sciencedirect.com/science/article/pii/S0022509622001302.

G. Cailletaud. A micromechanical approach to inelastic behaviour of metals. *International Journal of Plasticity*, 8:55–73, 1992.

Georges Cailletaud. *Une approche micromecanique phenomenologique du comportement inelastique des metaux*. PhD thesis, Paris univeristy Paris 6, 1987.

Jianqiang Chen. *Ductile tearing of AA2198 aluminium-lithium sheets for aeronautic application*. Theses, École Nationale Supérieure des Mines de Paris, April 2011.

C. C. Chu and A. Needleman. Void Nucleation Effects in Biaxially Stretched Sheets. *Journal of Engineering Materials and Technology*, 102(3):249–256, 07 1980. ISSN 0094-4289. doi: 10.1115/1.3224807. URL https://doi.org/10.1115/1.3224807.

Matthieu Dunand and Dirk Mohr. Optimized butterfly specimen for the fracture testing of sheet materials under combined normal and shear loading. *Engineering Fracture Mechanics*, 78(17): 2919–2934, 2011. ISSN 0013-7944. doi: https://doi.org/10.1016/j.engfracmech.2011.08.008. URL https://www.sciencedirect.com/science/article/pii/S0013794411003067.

Bjørn Håkon Frodal, Susanne Thomesen, Tore Børvik, and Odd Sture Hopperstad. On the coupling of damage and single crystal plasticity for ductile polycrystalline materials. *International Journal of Plasticity*, 142:102996, 2021. ISSN 0749-6419. doi: https://doi.org/10.1016/j.ijplas.2021.102996. URL https://www.sciencedirect.com/science/article/pii/S0749641921000711.

C. Gérard, B. Bacroix, M. Bornert, G. Cailletaud, J. Crépin, and S. Leclercq. Hardening description for fcc materials under complex loading paths. *Computational Materials Science*, 45(3):751–755, 2009. ISSN 0927-0256. doi: https://doi.org/10.1016/j.commatsci.2008.08.027. URL https://www.sciencedirect.com/science/article/pii/S0927025608003960. Proceedings of the 17th International Workshop on Computational Mechanics of Materials.

A. J. Gross and K. Ravi-Chandar. On the deformation and failure of Al 6061-T6 at low triaxiality evaluated through in situ microscopy. *International Journal of Fracture*, 200:185–208, 2016. ISSN 1573-2673. doi: https://doi.org/10.1007/s10704-016-0078-x.

A. L. Gurson. Continuum Theory of Ductile Rupture by Void Nucleation and Growth: Part I—Yield Criteria and Flow Rules for Porous Ductile Media. *Journal of Engineering Materials and Technology*, 99(1):2–15, 01 1977. ISSN 0094-4289. doi: 10.1115/1.3443401. URL https://doi.org/10.1115/1.3443401.

Sarra Haouala, Javier Segurado, and Javier LLorca. An analysis of the influence of grain size on the strength of fcc polycrystals by means of computational homogenization. *Acta Materialia*, 148:72–85, 2018. ISSN 1359-6454. doi: https://doi.org/10.1016/j.actamat.2018.01.024. URL https://www.sciencedirect.com/science/article/pii/S1359645418300557.

T. Hoc and S. Forest. Polycrystal modelling of if-ti steel under complex loading path. *International Journal of Plasticity*, 17(1):65–85, 2001. ISSN 0749-6419. doi: https://doi.org/10.

1016/S0749-6419(00)00019-X. URL https://www.sciencedirect.com/science/article/pii/S074964190000019X.

Anand Krishna Kanjarla, Paul Van Houtte, and Laurent Delannay. Assessment of plastic heterogeneity in grain interaction models using crystal plasticity finite element method. *International Journal of Plasticity*, 26(8):1220–1233, 2010. ISSN 0749-6419. doi: https://doi.org/10.1016/j.ijplas.2009.05.005. URL https://www.sciencedirect.com/science/article/pii/S0749641909000795. Special Issue In Honor of Lallit Anand.

A.P. Karafillis and M.C. Boyce. A general anisotropic yield criterion using bounds and a transformation weighting tensor. *Journal of the Mechanics and Physics of Solids*, 41(12):1859–1886, 1993. ISSN 0022-5096. doi: https://doi.org/10.1016/0022-5096(93)90073-O. URL https://www.sciencedirect.com/science/article/pii/002250969390073O.

Akhtar S. Khan and Muneer Baig. Anisotropic responses, constitutive modeling and the effects of strain-rate and temperature on the formability of an aluminum alloy. *International Journal of Plasticity*, 27(4):522–538, 2011. ISSN 0749-6419. doi: https://doi.org/10.1016/j.ijplas.2010.08.001. URL https://www.sciencedirect.com/science/article/pii/S0749641910001063.

Akhtar S. Khan and Haowen Liu. A new approach for ductile fracture prediction on al 2024-t351 alloy. *International Journal of Plasticity*, 35:1–12, 2012a. ISSN 0749-6419. doi: https://doi.org/10.1016/j.ijplas.2012.01.003. URL https://www.sciencedirect.com/science/article/pii/S0749641912000046.

Akhtar S. Khan and Haowen Liu. Strain rate and temperature dependent fracture criteria for isotropic and anisotropic metals. *International Journal of Plasticity*, 37:1–15, 2012b. ISSN 0749-6419. doi: https://doi.org/10.1016/j.ijplas.2012.01.012. URL https://www.sciencedirect.com/science/article/pii/S0749641912000137.

Akhtar S. Khan and Jian Liu. A deformation mechanism based crystal plasticity model of ultrafine-grained/nanocrystalline fcc polycrystals. *International Journal of Plasticity*, 86:56–69, 2016. ISSN 0749-6419. doi: https://doi.org/10.1016/j.ijplas.2016.08.001. URL https://www.sciencedirect.com/science/article/pii/S0749641916301280.

Xiang Kong. *Ductile damage study for low stress triaxiality and during load path changes via*

3D imaging and FE simulations. Theses, Université Paris sciences et lettres, June 2022. URL https://pastel.archives-ouvertes.fr/tel-04011202.

Xiang Kong, Lukas Helfen, Mathias Hurst, Daniel Hänschke, Djamel Missoum-Benziane, Jacques Besson, Tilo Baumbach, and Thilo F. Morgeneyer. 3d in situ study of damage during a 'shear to tension' load path change in an aluminium alloy. *Acta Materialia*, page 117842, 2022. ISSN 1359-6454. doi: https://doi.org/10.1016/j.actamat.2022.117842. URL https://www.sciencedirect.com/science/article/pii/S1359645422002282.

Xiang Kong, Jianqiang Chen, Yazid Madi, Djamel Missoum-Benziane, Jacques Besson, and Thilo Morgeneyer. Plasticity and ductility of an anisotropic recrystallized AA2198 Al-Cu-Li alloy in T3 and T8 conditions during proportional and non-proportional loading paths: simulations and experiments. *Journal of Theoretical, Computational and Applied Mechanics*, March 2023a. doi: 10.46298/jtcam.8913. URL https://jtcam.episciences.org/11078.

Xiang Kong, Djamel Missoum-Benziane, Fabrice Gaslain, Lukas Helfen, Mathias Hurst, Tilo Baumbach, Heikki Suhonen, and Thilo F. Morgeneyer. Ductile shear damage studied by correlative multiscale nanotomography and sem/ebsd for a recrystallized aluminium alloy 2198 t8. *Under preparation*, 2023b.

E. Kroner. Zur plastischen verformung des vielkristalls. *Acta Metallurgica*, 9(2):155–161, 1961. ISSN 0001-6160. doi: https://doi.org/10.1016/0001-6160(61)90060-8. URL https://www.sciencedirect.com/science/article/pii/0001616061900608.

P. Ladévèze. Sur la théorie de la plasticité en grands deformations. *Technical report, ENS Cachan*, 1980.

H. Li, M.W. Fu, J. Lu, and H. Yang. Ductile fracture: Experiments and computations. *International Journal of Plasticity*, 27(2):147–180, 2011. ISSN 0749-6419. doi: https://doi.org/10.1016/j.ijplas.2010.04.001. URL https://www.sciencedirect.com/science/article/pii/S0749641910000598.

H. Li, H.Q. Zhang, H. Yang, M.W. Fu, and Heng Yang. Anisotropic and asymmetrical yielding and its evolution in plastic deformation: Titanium tubular materials. *International Journal of Plasticity*, 90:177–211, 2017. ISSN 0749-6419. doi: https://doi.org/10.1016/j.ijplas.2017.01.004. URL https://www.sciencedirect.com/science/article/pii/S0749641917300293.

Yanshan Lou and Jeong Whan Yoon. Anisotropic yield function based on stress invariants for bcc and fcc metals and its extension to ductile fracture criterion. *International Journal of Plasticity*, 101:125–155, 2018. ISSN 0749-6419. doi: https://doi.org/10.1016/j.ijplas.2017.10.012. URL https://www.sciencedirect.com/science/article/pii/S0749641917303200.

Yanshan Lou, Saijun Zhang, and Jeong Whan Yoon. Strength modeling of sheet metals from shear to plane strain tension. *International Journal of Plasticity*, 134:102813, 2020. ISSN 0749-6419. doi: https://doi.org/10.1016/j.ijplas.2020.102813. URL https://www.sciencedirect.com/science/article/pii/S0749641919306230.

Meng Luo and Gilles Rousselier. Modeling of large strain multi-axial deformation of anisotropic metal sheets with strength-differential effect using a reduced texture methodology. *International Journal of Plasticity*, 53:66–89, 2014. ISSN 0749-6419. doi: https://doi.org/10.1016/j.ijplas.2013.07.006. URL https://www.sciencedirect.com/science/article/pii/S0749641913001435.

Komlanvi Madou and Jean-Baptiste Leblond. A gurson-type criterion for porous ductile solids containing arbitrary ellipsoidal voids—i: Limit-analysis of some representative cell. *Journal of the Mechanics and Physics of Solids*, 60(5):1020–1036, 2012a. ISSN 0022-5096. doi: https://doi.org/10.1016/j.jmps.2011.11.008. URL https://www.sciencedirect.com/science/article/pii/S0022509611002201.

Komlanvi Madou and Jean-Baptiste Leblond. A gurson-type criterion for porous ductile solids containing arbitrary ellipsoidal voids—ii: Determination of yield criterion parameters. *Journal of the Mechanics and Physics of Solids*, 60(5):1037–1058, 2012b. ISSN 0022-5096. doi: https://doi.org/10.1016/j.jmps.2012.01.010. URL https://www.sciencedirect.com/science/article/pii/S002250961200018X.

Komlanvi Madou and Jean-Baptiste Leblond. Numerical studies of porous ductile materials containing arbitrary ellipsoidal voids – i: Yield surfaces of representative cells. *European Journal of Mechanics - A/Solids*, 42:480–489, 2013. ISSN 0997-7538. doi: https://doi.org/10.1016/j.euromechsol.2013.06.004. URL https://www.sciencedirect.com/science/article/pii/S0997753813000697.

Komlanvi Madou, Jean-Baptiste Leblond, and Léo Morin. Numerical studies of porous ductile materials containing arbitrary ellipsoidal voids – ii: Evolution of the length and orientation of

the void axes. *European Journal of Mechanics - A/Solids*, 42:490–507, 2013. ISSN 0997-7538. doi: https://doi.org/10.1016/j.euromechsol.2013.06.005. URL https://www.sciencedirect.com/science/article/pii/S0997753813000703.

L. Méric, P. Poubanne, and G. Cailletaud. Single Crystal Modeling for Structural Calculations: Part 1—Model Presentation. *Journal of Engineering Materials and Technology*, 113(1):162–170, 01 1991. ISSN 0094-4289. doi: 10.1115/1.2903374. URL https://doi.org/10.1115/1.2903374.

T.F. Morgeneyer, J. Besson, H. Proudhon, M.J. Starink, and I. Sinclair. Experimental and numerical analysis of toughness anisotropy in aa2139 al-alloy sheet. *Acta Materialia*, 57(13):3902 – 3915, 2009. ISSN 1359-6454.

Thilo F. Morgeneyer, Thibault Taillandier-Thomas, Lukas Helfen, Tilo Baumbach, Ian Sinclair, Stéphane Roux, and François Hild. In situ 3d observation of early strain localization during failure of thin al alloy (2198) sheet. *Acta Materialia*, 69:78 – 91, 2014. ISSN 1359-6454.

Léo Morin, Jean-Baptiste Leblond, and Viggo Tvergaard. Application of a model of plastic porous materials including void shape effects to the prediction of ductile failure under shear-dominated loadings. *Journal of the Mechanics and Physics of Solids*, 94:148–166, 2016. ISSN 0022-5096. doi: https://doi.org/10.1016/j.jmps.2016.04.032. URL https://www.sciencedirect.com/science/article/pii/S0022509616302393.

Léo Morin, Jean-Baptiste Leblond, Dirk Mohr, and Djimédo Kondo. Prediction of shear-dominated ductile fracture in a butterfly specimen using a model of plastic porous solids including void shape effects. *European Journal of Mechanics - A/Solids*, 61:433–442, 2017. ISSN 0997-7538. doi: https://doi.org/10.1016/j.euromechsol.2016.10.014. URL https://www.sciencedirect.com/science/article/pii/S0997753816301176.

K. Nahshon and J.W. Hutchinson. Modification of the gurson model for shear failure. *European Journal of Mechanics - A/Solids*, 27(1):1 – 17, 2008. ISSN 0997-7538.

Kim L. Nielsen, Jonas Dahl, and Viggo Tvergaard. Collapse and coalescence of spherical voids subject to intense shearing: studied in full 3d. *International Journal of Fracture*, 177(2):97–108, 2012. ISSN 1573-2673. doi: 10.1007/s10704-012-9757-4.

Kim Lau Nielsen and Viggo Tvergaard. Failure by void coalescence in metallic materials containing primary and secondary voids subject to intense shearing. *International Journal of Solids and Structures*, 48(9):1255–1267, 2011. ISSN 0020-7683. doi: https://doi.org/10.1016/j.ijsolstr.2011.01.008. URL `https://www.sciencedirect.com/science/article/pii/S0020768311000175`.

Kedar S. Pandya, Christian C. Roth, and Dirk Mohr. Strain rate and temperature dependent fracture of aluminum alloy 7075: Experiments and neural network modeling. *International Journal of Plasticity*, 135:102788, 2020. ISSN 0749-6419. doi: https://doi.org/10.1016/j.ijplas.2020.102788. URL `https://www.sciencedirect.com/science/article/pii/S0749641919306722`.

Jessica Papasidero, Véronique Doquet, and Sebastien Lepeer. Multiscale investigation of ductile fracture mechanisms and strain localization under shear loading in 2024-T351 aluminum alloy and 36NiCrMo16 steel. *Materials Science and Engineering: A*, July 2014. doi: 10.1016/j.msea.2014.05.032. URL `https://hal.archives-ouvertes.fr/hal-01227265`.

Jessica Papasidero, Véronique Doquet, and Dirk Mohr. Ductile fracture of aluminum 2024-t351 under proportional and non-proportional multi-axial loading: Bao–wierzbicki results revisited. *International Journal of Solids and Structures*, 69-70:459–474, 2015. ISSN 0020-7683. doi: https://doi.org/10.1016/j.ijsolstr.2015.05.006. URL `https://www.sciencedirect.com/science/article/pii/S0020768315002164`.

Namsu Park, Thomas B. Stoughton, and Jeong Whan Yoon. A new approach for fracture prediction considering general anisotropy of metal sheets. *International Journal of Plasticity*, 124:199–225, 2020. ISSN 0749-6419. doi: https://doi.org/10.1016/j.ijplas.2019.08.011. URL `https://www.sciencedirect.com/science/article/pii/S0749641919300300`.

Tom Petit, Claire Ritter, Jacques Besson, and Thilo F. Morgeneyer. Impact of machine stiffness on "pop-in" crack propagation instabilities. *Engineering Fracture Mechanics*, 202:405–422, 2018. ISSN 0013-7944. doi: https://doi.org/10.1016/j.engfracmech.2018.08.007. URL `https://www.sciencedirect.com/science/article/pii/S0013794418305496`.

A. Pineau, A.A. Benzerga, and T. Pardoen. Failure of metals i: Brittle and ductile fracture. *Acta Materialia*, 107:424–483, 2016. ISSN 1359-6454.

F. Roters, P. Eisenlohr, L. Hantcherli, D.D. Tjahjanto, T.R. Bieler, and D. Raabe. Overview of constitutive laws, kinematics, homogenization and multiscale methods in crystal plasticity

finite-element modeling: Theory, experiments, applications. *Acta Materialia*, 58(4):1152–1211, 2010. ISSN 1359-6454. doi: https://doi.org/10.1016/j.actamat.2009.10.058. URL https://www.sciencedirect.com/science/article/pii/S1359645409007617.

Christian C. Roth and Dirk Mohr. Ductile fracture experiments with locally proportional loading histories. *International Journal of Plasticity*, 79:328–354, 2016. ISSN 0749-6419. doi: https://doi.org/10.1016/j.ijplas.2015.08.004. URL https://www.sciencedirect.com/science/article/pii/S0749641915001412.

Christian C. Roth, Thilo F. Morgeneyer, Yin Cheng, Lukas Helfen, and Dirk Mohr. Ductile damage mechanism under shear-dominated loading: In-situ tomography experiments on dual phase steel and localization analysis. *International Journal of Plasticity*, 109:169 – 192, 2018. ISSN 0749-6419.

G. Rousselier. Ductile fracture models and their potential in local approach of fracture. *Nuclear Engineering and Design*, 105(1):97–111, 1987. ISSN 0029-5493. doi: https://doi.org/10.1016/0029-5493(87)90234-2. URL https://www.sciencedirect.com/science/article/pii/0029549387902342.

G. Rousselier and S. Leclercq. A simplified "polycrystalline" model for viscoplastic and damage finite element analyses. *International Journal of Plasticity*, 22(4):685–712, 2006. ISSN 0749-6419. doi: https://doi.org/10.1016/j.ijplas.2005.04.011. URL https://www.sciencedirect.com/science/article/pii/S074964190500094X.

G. Rousselier, F. Barlat, and J.W. Yoon. A novel approach for anisotropic hardening modeling. part i: Theory and its application to finite element analysis of deep drawing. *International Journal of Plasticity*, 25(12):2383–2409, 2009. ISSN 0749-6419. doi: https://doi.org/10.1016/j.ijplas.2009.04.002. URL https://www.sciencedirect.com/science/article/pii/S0749641909000576.

G. Rousselier, F. Barlat, and J.W. Yoon. A novel approach for anisotropic hardening modeling. part ii: Anisotropic hardening in proportional and non-proportional loadings, application to initially isotropic material. *International Journal of Plasticity*, 26(7):1029–1049, 2010. ISSN 0749-6419. doi: https://doi.org/10.1016/j.ijplas.2010.01.001. URL https://www.sciencedirect.com/science/article/pii/S0749641910000021.

Gilles Rousselier. Finite deformation constitutive relations including ductile fracture damage. In *TRHEE-DIMENSIONAL CONSTITUTIVE RELATIONS AND DUCTILE FRACTURE*. North-Holland Publishing Company, 1981. URL https://hal-mines-paristech.archives-ouvertes.fr/hal-02060680.

Gilles Rousselier. Section 6.6 - the rousselier model for porous metal plasticity and ductile fracture. In JEAN LEMAITRE, editor, *Handbook of Materials Behavior Models*, pages 436–445. Academic Press, Burlington, 2001. ISBN 978-0-12-443341-0. doi: https://doi.org/10.1016/B978-012443341-0/50049-1. URL https://www.sciencedirect.com/science/article/pii/B9780124433410500491.

Gilles Rousselier. Porous plasticity revisited: Macroscopic and multiscale modeling. *International Journal of Plasticity*, 136:102881, 2021. ISSN 0749-6419. doi: https://doi.org/10.1016/j.ijplas.2020.102881. URL https://www.sciencedirect.com/science/article/pii/S0749641920304861.

Gilles Rousselier. Lode-dependent second porosity in porous plasticity for shear-dominated loadings. *International Journal of Plasticity*, 159:103446, 2022. ISSN 0749-6419. doi: https://doi.org/10.1016/j.ijplas.2022.103446. URL https://www.sciencedirect.com/science/article/pii/S0749641922002248.

Gilles Rousselier and Meng Luo. A fully coupled void damage and mohr–coulomb based ductile fracture model in the framework of a reduced texture methodology. *International Journal of Plasticity*, 55:1–24, 2014. ISSN 0749-6419. doi: https://doi.org/10.1016/j.ijplas.2013.09.002. URL https://www.sciencedirect.com/science/article/pii/S0749641913001745.

Gilles Rousselier, Meng Luo, and Dirk Mohr. Macroscopic plasticity modeling of anisotropic aluminum extrusions using a reduced texture methodology. *International Journal of Plasticity*, 30-31:144–165, 2012. ISSN 0749-6419. doi: https://doi.org/10.1016/j.ijplas.2011.10.004. URL https://www.sciencedirect.com/science/article/pii/S0749641911001689.

Gilles Rousselier, Thilo F. Morgeneyer, Sicong Ren, Matthieu Mazière, and Samuel Forest. Interaction of the portevin–le chatelier phenomenon with ductile fracture of a thin aluminum ct specimen: experiments and simulations. *International Journal of Fracture*, 206(1):95–122, Jul

2017. ISSN 1573-2673. doi: 10.1007/s10704-017-0203-5. URL https://doi.org/10.1007/s10704-017-0203-5.

K. Sai, G. Cailletaud, and S. Forest. Micro-mechanical modeling of the inelastic behavior of directionally solidified materials. *Mechanics of Materials*, 38(3):203–217, 2006. ISSN 0167-6636. doi: https://doi.org/10.1016/j.mechmat.2005.06.007. URL https://www.sciencedirect.com/science/article/pii/S0167663605000992.

Thomas B. Stoughton and Jeong Whan Yoon. A new approach for failure criterion for sheet metals. *International Journal of Plasticity*, 27(3):440–459, 2011. ISSN 0749-6419. doi: https://doi.org/10.1016/j.ijplas.2010.07.004. URL https://www.sciencedirect.com/science/article/pii/S0749641910000951.

Pouya Tajdary, Léo Morin, Liliana Romero-Resendiz, Maysam B. Gorji, Chedly Braham, and Gonzalo Gonzalez. Analysis of shear ductile damage in forming processes using a micromechanical model with void shape effects. *International Journal of Solids and Structures*, 248:111640, 2022. ISSN 0020-7683. doi: https://doi.org/10.1016/j.ijsolstr.2022.111640. URL https://www.sciencedirect.com/science/article/pii/S0020768322001627.

Thomas Tancogne-Dejean, Christian C. Roth, Thilo F. Morgeneyer, Lukas Helfen, and Dirk Mohr. Ductile damage of aa2024-t3 under shear loading: Mechanism analysis through in-situ laminography. *Acta Materialia*, 205:116556, 2021. ISSN 1359-6454.

C. Tekoglu and B. Koçhan. Unit cell calculations under fully characterized stress states. *International Journal of Plasticity*, 156:103358, 2022. ISSN 0749-6419. doi: https://doi.org/10.1016/j.ijplas.2022.103358. URL https://www.sciencedirect.com/science/article/pii/S0749641922001395.

V. Tvergaard and A. Needleman. Analysis of the cup-cone fracture in a round tensile bar. *Acta Metallurgica*, 32(1):157–169, 1984. ISSN 0001-6160. doi: https://doi.org/10.1016/0001-6160(84)90213-X. URL https://www.sciencedirect.com/science/article/pii/000161608490213X.

Viggo Tvergaard. Influence of voids on shear band instabilities under plane strain conditions. *International Journal of Fracture*, 17(4):389–407, Aug 1981. ISSN 1573-2673. doi: 10.1007/BF00036191. URL https://doi.org/10.1007/BF00036191.

Viggo Tvergaard. Shear deformation of voids with contact modelled by internal pressure. *International Journal of Mechanical Sciences*, 50(10):1459–1465, 2008. ISSN 0020-7403. doi: https://doi.org/10.1016/j.ijmecsci.2008.08.007. URL https://www.sciencedirect.com/science/article/pii/S0020740308001367.

Viggo Tvergaard. Behaviour of voids in a shear field. *International Journal of Fracture*, 158(1): 41–49, Jul 2009. ISSN 1573-2673. doi: 10.1007/s10704-009-9364-1. URL https://doi.org/10.1007/s10704-009-9364-1.

Liang Xue. Constitutive modeling of void shearing effect in ductile fracture of porous materials. *Engineering Fracture Mechanics*, 75(11):3343–3366, 2008. ISSN 0013-7944. doi: https://doi.org/10.1016/j.engfracmech.2007.07.022. URL https://www.sciencedirect.com/science/article/pii/S0013794407003220. Local Approach to Fracture (1986–2006): Selected papers from the 9th European Mechanics of Materials Conference.

Liang Xue and Tomasz Wierzbicki. Ductile fracture initiation and propagation modeling using damage plasticity theory. *Engineering Fracture Mechanics*, 75(11):3276–3293, 2008. ISSN 0013-7944. doi: https://doi.org/10.1016/j.engfracmech.2007.08.012. URL https://www.sciencedirect.com/science/article/pii/S0013794407003499. Local Approach to Fracture (1986–2006): Selected papers from the 9th European Mechanics of Materials Conference.

H. Yang, H. Li, H. Sun, Y.H. Zhang, X. Liu, M. Zhan, Y.L. Liu, and M.W. Fu. Anisotropic plasticity and fracture of alpha titanium sheets from cryogenic to warm temperatures. *International Journal of Plasticity*, 156:103348, 2022. ISSN 0749-6419. doi: https://doi.org/10.1016/j.ijplas.2022.103348. URL https://www.sciencedirect.com/science/article/pii/S0749641922001292.

J.W. Yoon, D.Y. Yang, and K. Chung. Elasto-plastic finite element method based on incremental deformation theory and continuum based shell elements for planar anisotropic sheet materials. *Computer Methods in Applied Mechanics and Engineering*, 174(1):23–56, 1999a. ISSN 0045-7825. doi: https://doi.org/10.1016/S0045-7825(98)00275-8. URL https://www.sciencedirect.com/science/article/pii/S0045782598002758.

J.W. Yoon, D.Y. Yang, K. Chung, and F. Barlat. A general elasto-plastic finite element formulation based on incremental deformation theory for planar anisotropy and its application to sheet metal forming. *International Journal of Plasticity*, 15(1):35–67, 1999b. ISSN 0749-6419. doi: https:

//doi.org/10.1016/S0749-6419(98)00059-X. URL https://www.sciencedirect.com/science/article/pii/S074964199800059X.

Zset. www.zset-software.com.